A Model Comparison of Different Flamelet Generated Manifolds for Analysis of Strained Hydrogen Flames

Jelle Kok

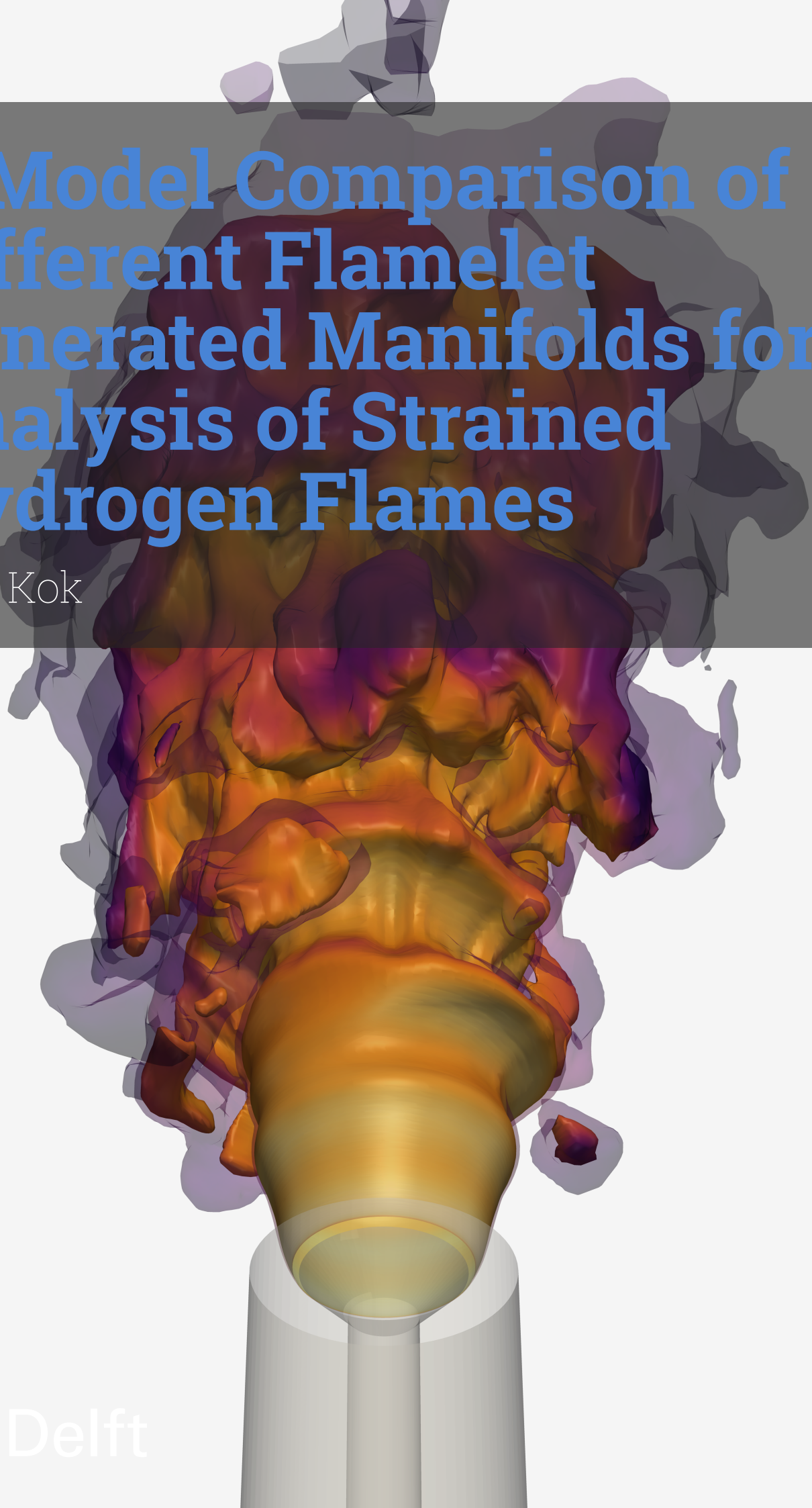

Delft University of Technology

TU Delft

A Model Comparison of Different Flamelet Generated Manifolds for Analysis of Strained Hydrogen Flames

by

Jelle Kok

to obtain the degree of Master of Science
at the Delft University of Technology,
to be defended publicly on Wednesday March 18, 2026 at 11:00 AM.

Responsible supervisor:	I. Langella
Supervisors:	A. Masucci
	A. Porcarelli
Project Duration:	April, 2025 - March, 2026
Faculty:	Faculty of Aerospace Engineering, Delft

Cover: Visualisation of results from this work

An electronic version of this thesis is available at `http://repository.tudelft.nl/`.

TU Delft

Preface

Dear reader,

Firstly, I would like to thank my supervisors for their guidance and the opportunity to learn more about this very interesting field in aerospace engineering, as well as for the opportunity to toy around with the very cool Snellius supercomputer.

I also would like to thank my friends for their support during the thesis and before that, without whom my life would be less bright. To the friends I met at the VSV, thank you for making my student life unforgettable and for enduring all those puns that usually only management 10 likes. To the friends from high school, thank you for the everlasting support. To the 2.56->6.19->SIM0.04 group, thank you for your attention when I just had to tell someone about how some things in OpenFOAM are just so unexpected, and for dragging me away from my desk to take a post-lunch mental health walk.

I also want to thank my family for their love and support. Through all things we have faced, you have been there for me, in person or in spirit.

Finally, I want to thank my girlfriend, for always being there for me, through the good and the bad. For letting me rant about a stupid bug in a python script. For enduring all the late nights I have spent on this and other projects. For pushing me to be the best I can be, but also for telling me to slow down when I get too stuck in something.

This report is the product of many months of work. During these months, I have learned much more than I ever thought I would about combustion modelling. It is also the final station of more than 8.5 years of studying aerospace engineering at the TU Delft. During that time, I have made friends for life and have learned many things about both aerospace engineering and myself, but now it is time for the next step.

Alles komt goed.

Jelle Kok
Delft, March 2026

Summary

Climate change is one of, if not the, defining issue of our time. In order to reduce humanity's dependency on fossil fuels, hydrogen is increasingly investigated as a promising energy carrier. When converting the chemical energy of hydrogen to the desired form, hydrogen reacts with oxygen to form water. This makes hydrogen very promising for achieving net-zero carbon emissions. For the aviation sector, hydrogen combustion has been suggested as a possible solution.

As with any technology, challenges remain. Whilst combustion modelling using Computational Fluid Dynamics (CFD) is not a solved problem to begin with, hydrogen combustion is made more complex by differential diffusion. This occurs when different species do not diffuse at the same rate. Hydrogen tends to diffuse faster than other species, causing local changes in mixture fraction, in addition to super-adiabatic temperatures and super-equilibrium product concentrations. This effect is stronger in strained or curved flames. Flame strain and curvature also influences the local reaction rate. These phenomena occur on a very small length and time scale. To simulate this directly, very fine meshes and very precise transport equations for each species are required. This can be prohibitively expensive for large scale designs or for design iteration.

In cases where simulating this behaviour directly is not possible, an alternative model is required. In this paper, five variants of such a model are assessed. These models are based on the assumption that the flame can be approximated as an ensemble of 1-dimensional flamelets. These flamelets can be analysed before the CFD simulations are performed. The results are then parametrized by a number of control variables, using a presumed filtered probability density function which aims to include sub-grid scale effects. By changing the flamelet conditions and control variables, different manifolds can be generated. In this paper, a number of these Flamelet-Generated Manifolds (FGMs) are compared to a higher fidelity model (using an Eulerian Stochastic Fields (ESF) approach). These FGMs use the mixture fraction, the progress variable and their sub-grid variances as control variables. Five different FGMs are tested, characterized by the progress variable definition (water vs hydrogen mass fraction) and flamelet strain rate (0 (unstrained) vs 3000 vs 6000 vs 13000 s^{-1}).

The performance of these models are assessed by means of a Large Eddy Simulation (LES) of a combustor with a bluff-body, using the open source CFD software OpenFOAM. The bluff-body causes a recirculation zone in its wake. Additionally, it causes a strain on the flame front, where differential diffusion is expected to cause super-adiabatic temperatures and super-equilibrium mixture fractions.

The results show that the FGMs give a good prediction of the conditionally averaged reaction rates. They are also capable of qualitatively predicting the increase in mixture fraction, super-adiabatic temperature and super-equilibrium product mass fractions. They can therefore be used in a strained combustor setting with lean, premixed hydrogen. However, there are challenges regarding the prediction of temperature, especially for FGMs using a hydrogen based progress variable. This should be investigated in the future. Furthermore, the FGMs predict the reaction rate well despite over-predicting the local effects of strain and differential diffusion.

Contents

Nomenclature

Acronyms

CCS Carbon Capture and Sequestration

CFD Computational Fluid Dynamics

DNS Direct Numerical Simulation

ESF Eulerian Stochastic Field

FDF Filtered Density Function

FGM Flamelet-Generated Manifold

GHG Greenhouse Gas

LES Large Eddy Simulation

PDF Probability Density Function

RANS Reynolds Averaged Navier-Stokes

SGS Sub-Grid Scale

SMR Steam Methane Reforming

TD Thermo-Diffusive

Symbols

Symbol	Definition	Unit
c	Progress variable	[-]
$\mathcal{D}$	Diffusivity	$[m^2 s^{-1}]$
h	Specific Enthalpy	$[J/kg]$
K	Flame stretch	$[s^{-1}]$
K_s	Tangential Strain rate	$[s^{-1}]$
K_c	Flame Curvature	$[s^{-1}]$
Le_i	Lewis number of species i	[-]
p	Pressure	$[Pa]$
R	Universal Gas constant	$[J/\text{mol}K]$
r	Radius	[m]
s_L	Laminar Flame speed	$[ms^{-1}]$
s_d	Displacement speed	$[ms^{-1}]$
T	Temperature	$[K]$
t	Time	$[s]$
U	Velocity	[m/s]
W_i	Molar mass of species i	$[g/\text{mol}]$
X_i	Molar fraction of species i	[-]
Y_i	Mass fraction of species i	[-]
y	Height	$[m]$
z	Mixture fraction	[-]
ρ	Density	$[\text{kg/m}^3]$
β_x	Diffusion coefficient for x	[arbitrary unit]
σ_c^2	Variance in progress variable	[arbitrary unit]
σ_z^2	Variance in mixture fraction	[arbitrary unit]
μ_t	Dynamic viscosity	$[kgm^{-1}s^{-1}]$

Symbol	Definition	Unit
ν_t	Kinematic viscosity	$[m^2 s^{-1}]$
ϵ_x	Scalar dissipation rate of parameter x	[-]
$\dot{\omega}_x$	Reaction rate for x	$[s^{-1}]$
θ_T	Normalized Temperature	[-]
Chemical symbols — Atoms		
H	Hydrogen	
O	Oxygen	
N	Nitrogen	
C	Carbon	
Chemical symbols — Molecules		
H_2	Hydrogen	
O_2	Oxygen	
H_2O	Water	
N_2	Nitrogen	
NO_x	Nitrogen Oxides	
NO	Nitric Oxide	
NO_2	Nitrogen Dioxide	
CO_2	Carbon Dioxide	
CH_4	Methane	

List of Figures

List of Tables

1 Introduction

1.1. Need for new energy carriers

Climate change is one of, if not the, defining issue of this time. It could lead to more severe weather events and longer, more severe droughts. This in turn leads to food and water shortages, potentially leading to national or even global conflicts. Additionally, global warming can lead to a sea level rise. All of these factors can lead to the displacement of potentially millions of people [1]. It is nearly indisputable that the current effects of climate change are caused by human behaviour [2], mainly due to our energy use and the way this energy is produced. As a society, we use an incredible amount of energy each year, most of which is produced using fossil fuels (coal, natural gas and oil). In 2023, more than 80% of the global energy production was produced using fossil fuels [3].

The impact society has on the climate can be reduced in a number of ways. We can emit less Greenhouse Gas (GHG) by reducing our energy usage. We can also use Carbon Capture and Sequestration (CCS). This is the process of capturing and storing CO_2, either directly at the source or from the atmosphere [4]. Furthermore, we can emit less GHG by changing the way the energy is produced. The latter can be achieved by transitioning from fossil fuels to energy produced using other sources. This could be electricity generated using carbon-free sources, such as wind, solar, nuclear or hydropower.

Whilst electrification is possible for many systems, there are a number of energy use cases where this is not easily possible. For instance, it is expected that combustion will continue to be used as a power source in aviation, due to the higher specific energy of fuels compared to batteries.

A drawback of renewable energy is that supply is decoupled from demand. This can lead to overproduction of energy on sunny and/or windy days and moments where demand might be larger than the supply. To solve this, the excess energy during times of high supply could be stored in some way, and converted to electrical energy when required. Another drawback is the fact that it is very costly, if not impossible, to transport electrical energy over large distances. These two challenges could be solved if the electrical energy could used to convert chemical species into other species with a higher enthalpy of formation. The species can then be stored and used at a later time. Additionally, they can also be transported over larger distances, for instance by ship or by pipelines.

1.2. Hydrogen Opportunities and Challenges

Hydrogen seems to be very promising for converting electrical energy to chemical energy. Using electrolysis, water (H_2O) can be separated into oxygen (O_2) and hydrogen (H_2). The resulting hydrogen can then either be used directly, or be used to convert other species.

1.2.1. Opportunities

No CO_2 emissions

Whist the processes differ significantly, the global reaction for hydrogen combustion and hydrogen fuel cells is the same. In both cases, hydrogen and oxygen react exothermally, only forming water. The one

step global reaction is $H_2 + 0.5\,O_2 \longrightarrow H_2O$. In both cases, no CO_2 is produced.

Production
Hydrogen can be produced in a number of ways. As mentioned in section 1.1, it can be produced using electrolysis. This can be a way of reducing the overproduction of (renewable) electricity.

Hydrogen can also be produced from fossil fuels, for instance from methane pyrolysis. In this process, a hydrocarbon such as methane (CH_4) is heated up in an environment without oxygen, causing the molecules to split and form hydrogen and solid carbon ($CH_4 \longrightarrow 2\,H_2 + C$). The excess carbon can be used for other processes. Whilst no CO_2 is directly produced by this method, CO_2 can be produced during heat generation. Hydrogen can also be produced using Steam Methane Reforming (SMR). In this process, methane and steam react to form carbon monoxide and hydrogen ($CH_4 + H_2O$ (g) $\rightleftharpoons$ CO + $3\,H_2$). The carbon monoxide can then react again with steam to form CO_2 and hydrogen (CO^+H_2O (g) $\rightleftharpoons$ $CO_2 + H_2$) [5]. The CO_2 can be captured using CCS.

Another way of hydrogen production is thermolysis of H_2O, where water is subjected to a very large temperature, causing it to split and form hydrogen and oxygen [6]. The source of thermal energy could potentially be a nuclear reactor or concentrated solar power. This method comes with additional risks, as you now have fuel, oxygen and a high temperature. Great care is required to prevent disasters.

Hydrogen also occurs naturally in underground pockets. This can be a relatively cheap source of hydrogen. Hydrogen is produced continuously in the earths crust. In locations where the concentration and production rates are high, a well can be constructed to extract the gas to the surface [7].

Energy Security
Globally, fossil fuels deposits are not distributed uniformly. Many countries do not have direct access to (sufficient) fossil fuels within their borders, and thus need to import it from other sources. This gives exporting countries a significant political and financial leverage over importing countries, e.g. by means of an oil emargo such as the 1973 oil crisis [8].

Hydrogen production, especially if produced by electrolysis using renewable energy, can help reduce this dependency. The hydrogen production can be used to increase the utilisation of the installed renewable energy systems in case of overproduction, and reduce the need for fossil fuels in the cases where production of electricity is low.

1.2.2. Challenges
There are a number of challenges to be solved before hydrogen can really compete with fossil fuels.

Storage and Transport
Due to a number of factors, hydrogen is difficult to store and transport.

Low volumetric energy density: Whilst hydrogen has one of the highest specific energies, it is also one of the lowest density substances. Due to the low density, it is nearly required that hydrogen is either compressed to very high pressures (600 to 700 bars) or liquefied at a temperature of approximately 20 K. Even then, the volumetric energy density is significantly lower than other fuels, as shown in Figure 1.1.

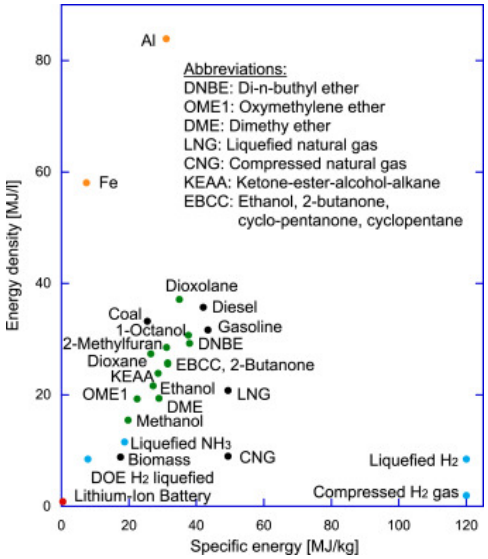

Figure 1.1: Mass and volumetric energy densities of different fuels, adapted from Pitsch, [9]

In order to transfer the same amount of energy in a pipeline, a higher volumetric flow rate is required. Similarly, a much larger volume is needed to store the same amount of energy, requiring larger structures. The structures should also be very resilient to high pressures when gaseous hydrogen is used, and be very well isolated for the use of liquified hydrogen. This additional structural weight negates the very high specific energy of hydrogen. For aircraft, the larger tanks also lead to more drag, either by increasing the frontal area, or by increasing the wetted surface which increases skin friction. If it is chosen to increase the fuselage length to fit the tank, the aircraft might also be too long to service some airports.

Interaction with structures: Hydrogen can permeate into the walls of storage vessels or transport pipes [10]. This can also weaken steel structures by means of 'hydrogen embrittlement' [11]. This means that existing storage and transport facilities for hydrocarbon fuels cannot easily be reused for hydrogen.

Safety: Hydrogen ignition can occur for a wide range of air-hydrogen mixture ratios. Additionally, hydrogen is color- and odorless, so it is difficult to detect. Hydrogen flames are also invisible to the naked eye [12]. The storage of hydrogen also mainly occurs at very high pressures or very low temperatures, which can both cause severe harm.

Costs

Currently, hydrogen is more expensive to produce than fossil fuel [13].

Hydrogen flame characteristics

Hydrogen combustion, especially in turbulent and premixed conditions, is more complex than hydrocarbon combustion. Since hydrogen has a very high mass diffusivity compared to the heat diffusivity, molecular transport continues to play a significant role on the characteristics of the combustion process [14]. To accurately model this behaviour, complex (and thus costly) models are required. This makes design optimization difficult. These challenges are explained in more detail in chapter 2.

High NO_x emissions

NO_x is a shorthand for the nitrogen oxides NO and NO_2. Both are harmful to both health [15] and the environment, e.g. through its large greenhouse potential [16]. There are a number of ways in which NO_x are formed. For hydrogen combustion, the most relevant formation method is thermal NO_x, where atomic nitrogen and oxygen in the air react (endothermically) under a very high temperature. The reaction rate is dependent on a number of factors, such as temperature and residence time [17]. Since the adiabatic flame temperature tends to be higher for hydrogen combustion, NO_x production is consequentially higher as well.

NO_x emissions can be reduced in a number of ways. The exhaust mixture can be fed through a catalytic converter, but this is not always feasible. The flame temperature can also be reduced. One way to achieve this is to mix the hydrogen and air before combustion (i.e. premixed) below the stoichiometric fuel-air ratio (i.e. lean). This way, the adiabatic flame temperature can be reduced significantly [18].

2

Hydrogen Combustion

There are a number of differences between hydrocarbon and hydrogen combustion. In hydrogen combustion, there are inherently less unique reactions and species involved. There are no reactions or species involving carbon, and the molecules tend to consist of a low number of atoms.

2.1. Types of combustion

There are a number of different ways to characterise flames. Such as whether or not the fuel and air are mixed before the combustion, if the mixture is rich or lean or if the surrounding flow is laminar or turbulent. For different applications, different types of flame offer better performance.

Premixed combustion

In premixed conditions, the fuel and air are mixed before the reaction zone. In non-premixed combustion, the flame front occurs in the place where stoichiometric conditions are reached, even if the fuel to air ratio might not be stoichiometric. However, at stoichiometric conditions the temperature is high. When the fuel and oxidizer streams are mixed before the reaction occurs, the equivalence ratio and thus the temperature can be controlled. Reducing the peak temperature can be beneficial for reducing the NO_x emissions.

There are drawbacks to premixed combustion as well. If the local burning and flow velocities are not opposite but equal, the flame front will move. If the flame speed is lower than the flow velocity, the flame can be "blown off", which can extinguish the flame. On the other hand, a higher flame speed can 'flash-back' into the inlet, which can damage the structure. Due to the relatively high flame speed of hydrogen flames, flash-back is a significant challenge.

Turbulent combustion

Turbulence has a strong influence on the behaviour of flames. The smallest eddies can have an effect on the flame surface. This causes the flame front to wrinkle, increasing the surface area. The wrinkles also lead to Thermo-Diffusive (TD)-instabilities in the case of hydrogen combustion. This can significantly increase the fuel consumption rate. The synergistic relation of TD-instabilities and turbulence have been shown numerically by Berger et al, [14]. It is shown that fuel consumption rate is increased more than either flame wrinkling or TD-instabilities cause individually.

Flame stretch & Lewis number

Flames can also be characterized by the stretch of the flame surface. This change is quantified by the flame stretch K. K is defined as $K = \frac{1}{A}\frac{\mathrm{d}A}{\mathrm{d}t}$, where A is the area of the flame surface. Flame stretch can occur due to a curvature of the flame front, as well as by a strain rate of the flow field.

Flame stretch can have a significant influence on the behaviour of a flame. This is partially caused by a difference in heat transport to the pre-heat region before. In a region where the flame is concave towards the unburned flow, the reactants are surrounded by the flame, leading to more thermal energy being

transported to the pre-heat region. The opposite occurs for a convex flame.

The effect of a positive or negative stretch on parameters like the flame speed depends (amongst other things) on the fuel. Different species in premixed flows can have a different ratio of thermal and mass diffusivity. This ratio is called the Lewis number. The effect this phenomenon has on hydrogen combustion is explained in section 2.2.

2.2. Instabilities

Non-unity Lewis number

A significant difference between hydrogen and hydrocarbon flames is caused by the non-unity Lewis number of hydrogen ($Le_{H_2} \approx 0.3$). The Lewis number is the ratio of the thermal diffusivity to the mass diffusivity. Due to inherent perturbations, certain regions in the flame surface may be slightly richer than others. Since the thermal diffusivity is lower than the mass diffusivity of hydrogen, more chemical energy is brought to this region than thermal energy can be transported to the preheat region. This leads to a local increase in temperature, which increases the reaction speed and the laminar flame speed, which causes the perturbation to grow in size. Additionally, the increase in temperature causes more hydrogen to be "sucked into" this region, causing a positive feedback loop [9].

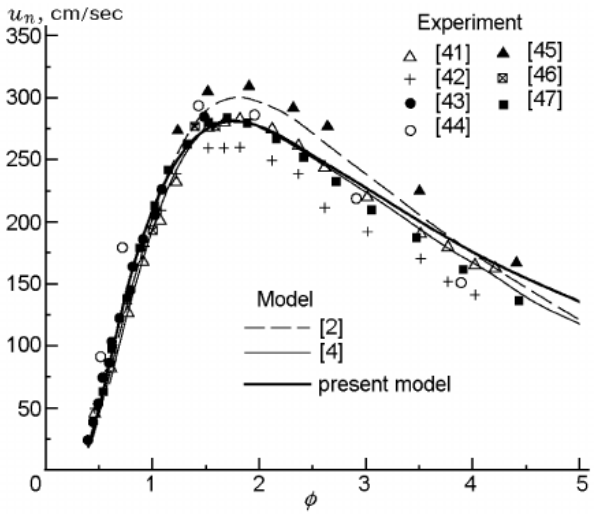

Figure 2.1: Laminar flame speed at different fuel to air ratios for H_2-air flames, from [19]

Flame stretch

Hydrogen flames also have a different relation with flame stretch compared to hydrocarbon flames. Flame stretch is the rate of change of flame surface area. This change can occur due to the flow field, for instance in a vortex, or due to wrinkles in the flame front such as the ones caused by TD-instabilities. Below equivalence ratios of around 0.8, the laminar flame speed of hydrogen has a positive dependency on flame stretch [20]. In other words, more flame stretch can lead to higher flame speeds. The higher flame speed can then increase the size of the perturbations.

Combined effect

Both the non-unity Lewis number and the positive effect of flame stretch on the flame speed can play a role simultaneously. The combined effect is often referred to as TD-instability [14]. TD-instabilities influence the fuel consumption rate in two ways [14]. The flame surface is increased, and the laminar burning velocity is increased locally, so each unit of flame surface consumes more fuel.

The interaction between flame stretch and differential diffusion also leads to local super-equilibrium conditions. This means that the mixture fraction, flame temperature and reaction products might locally be higher than the inlet conditions suggest [14]. The increase in mixture fraction and temperature also increase the local reaction rate, which in turn leads to a change in flame shape and flow field. This can increase the local strain rate, leading to even higher mixture fractions and temperatures.

Modelling challenges

Modelling reacting flows is complex. The length and time scales involved are very small, requiring very fine meshes. The thermophysical properties that determine the reactions can change due to a difference in chemical composition, due to the change in temperature, or even due to a change in the flow field. These relations are often not linear. Hydrogen combustion is further complicated by TD-instabilities. These have a significant effect on the behaviour of the flame [14], and occur on a very small length scale, often smaller than the mesh size. Modelling this requires more complex models compared to hydrocarbon combustion models.

3

Numerical Hydrogen Combustion Modelling

Combustion modelling is complex, as there is a strong interaction between the flow and the flame. The large number of (reacting) species further increases the complexity. Hydrogen combustion is even more complex, due to small-scale effects such as differential diffusion.

3.1. Combustion Modelling

There are a number of different ways of modelling combustion. Methods are often based on solving the Navier-Stokes equations, with additional models providing the needed closure.

3.1.1. Fluid field modelling

To determine the (3D) flow field surrounding the combustion, Computational Fluid Dynamics (CFD) is often used. Most models use either a Direct Numerical Simulation (DNS) (very high fidelity, but very high cost), Large Eddy Simulation (LES) (lower fidelity and cost compared to DNS), or Reynolds Averaged Navier-Stokes (RANS) (lower fidelity and cost compared to LES and DNS). DNS works by resolving the domain at the scale of the smallest eddies in both length and time. This leads to a very fine mesh, which also requires a very small time step. LES is similar to DNS in method, but now only the largest scale eddies are resolved. For the smaller scales, a model is used to predict the behaviour of the Sub-Grid Scale (SGS). RANS models work in a different way. In RANS-based models, it is assumed that the turbulent fluctuations can be averaged out, providing a steady-state, time-averaged flow field. It is computationally efficient, but there are no resolved states and many characteristics that depend on interaction with turbulence, such as TD-instabilities, cannot be predicted.

3.1.2. Combustion models

Beside a number of different CFD archetypes, there are a large number of different types of combustion models, varying in computational cost and accuracy.

Detailed chemistry

A detailed chemistry models aims to include most, if not all, of the reactions that occur in the combustion. This also requires knowing the local concentration of all sub-species, which might be influenced by molecular diffusion or be transported by the flow. The concentration will also change as the species react. This can be done by writing transport equations for each species, with source terms based on the reactions that occur. However, there are often many species and reactions involved (9 for hydrogen-air combustion [21], 53 for CH_4-air, even more for larger molecules). This means that many transport equations are required. The computational load can be reduced by not resolving all reactions. If the overall reaction mechanism is mainly defined by some reactions, it could be possible to only resolve those. However, the computational cost of (reduced) detailed chemistry models tends to be very high. They are usually used for academic purposes, or for validation of lower fidelity models.

Tabulated chemistry
This method aims to reduce the computational cost by mapping the chemistry to lower-dimension manifolds. The chemistry is parametrized based on a number of control variables. Often, the chemical composition or mixture fraction is used in combination with a progress variable. By first determining the characteristics of the chemical reaction(s) for the full range of control variables, a look-up table can be constructed for each parameter of interest. During the simulation, only the transport equation for the control variables and Navier-Stokes equations need to be resolved, after which the other parameters can be interpolated from the manifolds. Mutual interactions between the control variables and the tabulated parameters can still be taken into account by including the parameters into the transport equations and using and iterating until convergence is achieved. Compared to detailed chemistry, there are significantly less transport equations to be solved. Additionally, the interpolation is likely faster than solving the system of chemical reactions. These aspects can lead to a significant decrease in computational load.

When constructing the manifolds, great care needs to be used when selecting the control variables. The conditions for which the manifolds are generated also influence the tabulated data. Additionally, the model might not be able to capture some effects, as species concentration is not often not resolved. The manifolds are also bound by the pre-determined control variable states, as interpolation is not possible outside of these states.

Flamelet Generated Manifolds Flamelet-Generated Manifolds (FGMs) are an example of tabulated chemistry. They depend on the assumption that whilst a turbulent flame can affect the flame front, it does not affect the inner structure of the flame. A turbulent flame can therefore be approximated as an ensemble of 1-dimensional laminar flames [22], called flamelets. These flamelets can be used to construct the manifolds for the tabulated chemistry model. This is explained in greater detail in section 3.2.

Probability Density Function methods
Probability Density Function (PDF)-based methods use a transport equation for the joint PDF of a set of scalars. This set can contain scalars such as mixture fraction and the mass fraction of the relevant species. The main advantage of this method is that non-linear SGS effects can still be captured. This is done by solving the transport equation for the Filtered Density Function (FDF). The turbulence-chemistry interaction does not have to be solved exactly. Instead, the chemical source terms are evaluated by finding the expected value of the source terms. These are then used to update the transport equation of the PDF.

Lagrangian PDF methods Lagrangian PDF methods represent the PDF using many stochastic particles. These particles all carry its own set of scalars, for which the transport equations are solved. This gives very accurate results, where SGS effects can be taken into account. However, a very large number of particles is required for statistical convergence, leading to a very high computational cost [23]. Especially for 3D simulations, this can be prohibitively expensive.

Eulerian PDF methods Eulerian PDF methods use stochastic fields instead of stochastic particles. Here, transport equations are solved for a finite number of stochastic fields. The ensemble of the fields are then used to approximate the PDF

PDF-FGM models
PDF and FGM methods can be combined into a combined model. Instead of using transport equations for the control variables directly, a joint PDF is used instead. Contrary to the PDF methods described above, the joint PDF only needs to contain the control variables, leading to a low-dimensional PDF. By using the FDF a part of the turbulence-chemistry interaction on the SGS level can still be captured, at a lower computational cost compared to the full PDF methods described above.

FGM-based models can also use a PDF approach to reduce the uncertainty in the manifolds. This is done by determining the conditional mean of the PDF of the tabulated parameters, as determined by the 1-dimensional simulation, at each possible state of the control variables [22]. In Equation 3.1, this method is shown for an arbitrary parameter ξ.

$$\overline{\xi}(z,c,\sigma_z^2,\sigma_c^2) = \overline{\rho}\int_0^1\int_0^1 \frac{\xi(z,c)}{\rho(z,c)} P(z,c;\widetilde{z},\widetilde{c},\sigma_z^2,\sigma_c^2)dzdc \tag{3.1}$$

3.2. Models used in this work

The models used in this work is a PDF-FGM model, where the PDF is used for reducing uncertainty in the manifolds. The control variables used for the manifolds are the mixture fraction z, the progress variable c, and their variances σ_z^2 and σ_c^2. Presumed PDFs using a Beta distribution is used. The shape of these Beta distributions is determined from the filtered value ($\widetilde{z}$ or $\widetilde{c}$) and its sub-grid variance ($\widetilde{\sigma_z^2}$ or $\widetilde{\sigma_c^2}$), in line with previous studies [22].

3.2.1. Definition of control variables

Mixture fraction The mixture fraction is used to quantify the local ratio between hydrogen and oxygen. It is bound between 0 (only air) and 1 (only fuel). It is quantified as Equation 3.2. Here, W_i refers to the molar mass of species i. z_H and z_O are the hydrogen and oxygen atom mass fraction. Subscripts 1 and 2 for z_i refer to the fuel and oxidiser streams. The constant values used are $z_{H,1} = 1$, $z_{H,2} = 0$, $z_{O,1} = 0$ and $z_{O,2} = 0.23$. In this case, the fuel and oxidiser streams are assumed to have mixed completely before entering the numerical domain.

$$z = \frac{0.5W_{\mathrm{H_2}}(z_{\mathrm{H}} - z_{\mathrm{H},2}) - W_{\mathrm{O_2}}^{-1}(z_{\mathrm{O}} - z_{\mathrm{O},2})}{0.5W_{\mathrm{H_2}}(z_{\mathrm{H},1} - z_{\mathrm{H},2}) - W_{\mathrm{O_2}}^{-1}(z_{\mathrm{O},1} - z_{\mathrm{O},2})} \tag{3.2}$$

Progress variable The progress variable c is used to quantify to what extend the combustion is completed. There are a number of ways in which c can be determined, but most methods rely on comparing a local parameter to the value of that parameter at the end or start of the combustion progress. This could be for instance the concentration of a certain species, for instance H_2 concentration [14]. In that paper, $c = 1 - \frac{Y_{\mathrm{H_2}}}{Y_{\mathrm{H_2},unburned}}$ is used. As the concentration of H_2 reduces during the combustion process, the progress variable increases. It approaches 1 as the combustion is complete. Another species-based progress variable is the concentration of H_2O, i.e. $c = \frac{Y_{\mathrm{H_2O}}}{Y_{\mathrm{H_2O},burned}}$ [24]. Other parameters, such as temperature can also be used [25]. In this paper, FGMs using H_2 and H_2O based progress variables are compared.

The H_2O based progress variable $c_{\mathrm{H_2O}}$ is defined according to Equation 3.3. The superscripts *reac* and *prod* refer to the mass fraction in the unburned and burned sections respectively. To account for changes in the mass fraction due to the expected changes in mixture fraction, the mass fractions are functions of z.

$$c = c_{\mathrm{H_2O}} = \frac{\Delta Y_{\mathrm{H_2O}(z)}}{\psi_{\max}(z)} = \frac{Y_{\mathrm{H_2O}}(z) - Y_{\mathrm{H_2O}}^{reac}(z)}{Y_{\mathrm{H_2O}}^{prod}(z) - Y_{\mathrm{H_2O}}^{reac}(z)} \tag{3.3}$$

Additionally, a H_2 based progress variable is used, which is defined according to Equation 3.4.

$$c_{\mathrm{H_2}} = 1 - \frac{Y_{\mathrm{H_2}}}{Y_{\mathrm{H_2},unburned}(z)} \tag{3.4}$$

3.2.2. Tabulating method

The tabulated parameters are determined as shown in Equation 3.5, where $\overline{x}$ represents the tabulated scalar, x the scalar as determined by the 1-dimensional simulations, ρ the density and $P(c,z;\widetilde{c},\widetilde{z},\sigma_c^2,\sigma_z^2)$ the conditional probability density function at a given control variable state.

$$\overline{x}(c,z,\sigma_c,\sigma_z) = \overline{\rho}\int_0^1\int_0^1 \frac{x_c(c,z)}{\rho(c,z)} P(c,z;\widetilde{c},\widetilde{z},\sigma_c^2,\sigma_z^2)dcdz \tag{3.5}$$

3.2.3. Transport equations

The following transport equation for the Favre-filtered $\widetilde{z}$ is used, in line with previous studies [22]:

$$\overline{\rho}\frac{D\widetilde{z}}{Dt} = \nabla \cdot \frac{\mu_t}{Sc_t}\nabla\widetilde{z} + \nabla \cdot \overline{\rho}\widetilde{\mathcal{D}}\nabla\widetilde{\beta_z} \tag{3.6}$$

In Equation 3.6, μ_t is the dynamic viscosity, Sc_t is the laminar Schmidt number. The filtered diffusivity $\widetilde{\mathcal{D}}$ and the coefficient $\widetilde{\beta_z}$ are obtained from the FGM interpolation.

The transport equation for the Favre-filtered $\widetilde{c}$ is described below:

$$\overline{\rho}\frac{D\widetilde{c}}{Dt} = \nabla \cdot \frac{\mu_t}{Sc_t}\nabla\widetilde{c} + \nabla \cdot \overline{\rho}\widetilde{\mathcal{D}}\nabla\widetilde{\beta_c} + \overline{\dot{\omega}_c} \tag{3.7}$$

In the equations above, The filtered diffusivity $\widetilde{\mathcal{D}}$, the coefficient $\widetilde{\beta_c}$ and the progress variable source term $\dot{\omega}_c$ are obtained from the FGM interpolation.

The variance of the mixture fraction is transported according to Equation 3.8. Here, $\widetilde{\epsilon_z}$ is the scalar dissipation rate.

$$\overline{\rho}\frac{D\widetilde{\sigma_z^2}}{Dt} = \nabla \cdot [(\overline{\rho\mathcal{D}} + \frac{\mu_t}{Sc_t})\nabla\widetilde{\sigma_z^2}] - 2\overline{\rho}\widetilde{\epsilon_z} + 2\frac{\mu_t}{Sc_t}(\nabla\widetilde{z} \cdot \nabla\widetilde{z}) \tag{3.8}$$

The variance of the progress variable is transported according to Equation 3.9. $\overline{c\dot{\omega}_c}$ is obtained from the FGM.

$$\overline{\rho}\frac{\mathrm{D}\widetilde{\sigma_c^2}}{\mathrm{D}t} = \nabla \cdot [(\overline{\rho\mathcal{D}} + \frac{\mu_t}{Sc_t})\nabla\widetilde{\sigma_c^2}] - 2\overline{\rho\epsilon}_c + 2\frac{\mu_t}{Sc_t}(\nabla\widetilde{c} \cdot \nabla\widetilde{c}) + 2(\overline{c\dot{\omega}_c} - \widetilde{c}\dot{\omega}_c) \tag{3.9}$$

The transport equation for enthalpy is given by Equation 3.10. $\widetilde{\beta_{h_1}}$ and $\widetilde{\beta_{h_2}}$ are retrieved from the manifold interpolation.

$$\overline{\rho}\frac{\mathrm{D}\widetilde{h}}{\mathrm{D}t} = \nabla \cdot (\frac{\mu_t}{Pr_t})\nabla\widetilde{h} + \nabla \cdot (\overline{\rho}\widetilde{\mathcal{D}}\widetilde{\beta_{h_1}}\nabla\widetilde{T} + \overline{\rho}\widetilde{\mathcal{D}}\nabla\widetilde{\beta_{h_2}}) \tag{3.10}$$

3.2.4. FGM databases

In this paper, 5 FGMs are compared. These consist of 1 FGM with an H_2O based progress variable and 4 FGMs with an H_2 based progress variable. The H_2O and one of the H_2 based FGMs are constructed using unstrained flamelets. The remaining three FGMs use flamelets with a constant strain rate of 3000, 6000 and 13000 s^{-1} respectively. Other than the definition of the progress variable, the FGMs all use the same control variables.

FGM	progress variable	Strain rate [s^{-1}]
FGM A	c_{H_2O}	0
FGM B	c_{H_2}	0
FGM C	c_{H_2}	3000
FGM D	c_{H_2}	6000
FGM E	c_{H_2}	13000

Table 3.1: FGMs used in this work

For the c_{H_2O} based FGM, there are no cases where a strain rate is applied. In cases with strained flames, differential diffusion effects will cause a change in mixture fraction locally. This can cause the peak of the H_2O mass fraction to occur before the combustion is complete. This would result in a non-monotonic

progress variable, which either exceeds 1 at the peak mass fraction, or settles at a value lower than 1. This makes interpolation impossible.

The following parameters are tabulated in all FGMs:

- Specific heat capacity C_p
- Enthalpy of formation Δh_f^0
- Mixture molar mass W
- Progress variable production rate $\dot{\omega}_c$
- Progress variable production rate times progress variable $c\dot{\omega}_c$
- d2Y
- YMax
- β_c
- β_z
- $\mathcal{D}$
- β_{h_1}
- β_{h_2}

In Figure 3.1, the average value for $\dot{\omega}_c$ from the FGM table can be found.

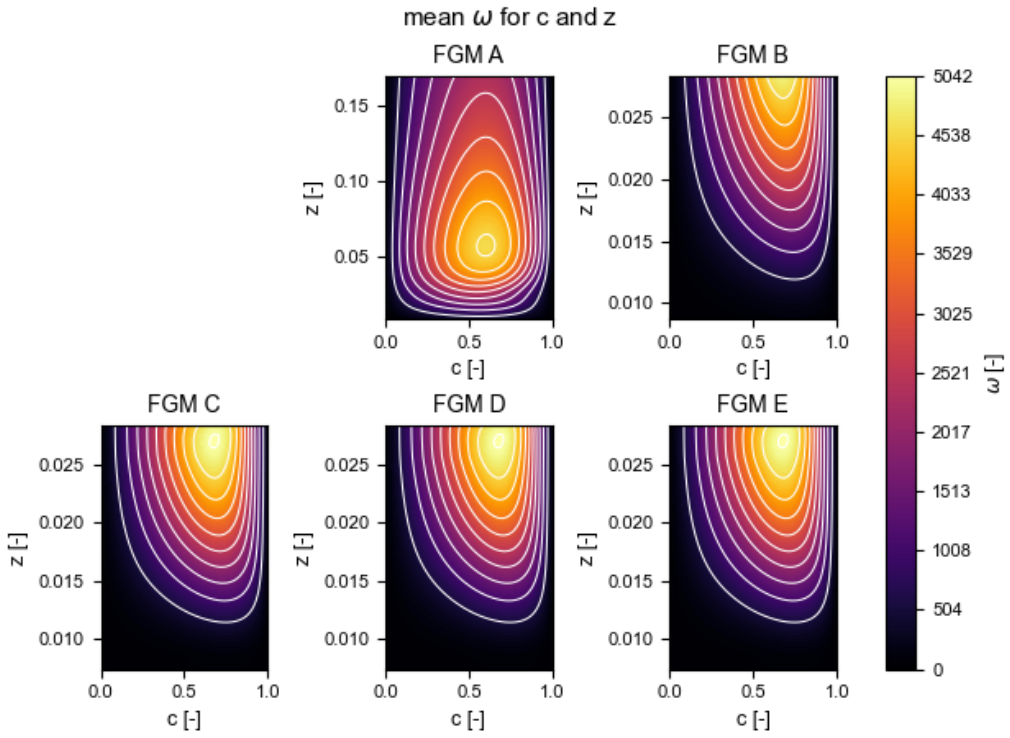

Figure 3.1: Average $\dot{\omega}_c$ from the FGM tables

The filtered temperature $\widetilde{T}$ is determined using Equation 3.11. $T_0 = 298.15$ K.

$$\widetilde{T} = T_0 + \frac{(\widetilde{h} + \widetilde{\Delta h_f^0})}{\widetilde{C_p^{\text{eff}}}} \tag{3.11}$$

This is then used to compute the local mixture density by means of the ideal gas law Equation 3.12.

$$\overline{\rho} = \frac{p\widetilde{W}}{R_0\widetilde{T}} \tag{3.12}$$

3.3. Numerical implementation of the models

3.3.1. FGM Interpolation

Each tabulated parameter is stored in a flattened list of length $n_z \cdot n_c \cdot n_{\sigma_z^2} \cdot n_{\sigma_c^2}$. In order to determine the correct values from this list, first the correct indices and interpolation factors needs to be found. z, c and σ_c^2 use a linear spacing. The index i for these variables can be found by multiplying the normalized local value of variable x by $(n_x - 1)$, then converting this number to an integer value and finally adding 1. This is shown mathematically in Equation 3.13. The resulting index is the index of the closest higher value. The actual value of x can thus be found between $x'[i-i]$ and $x'[i]$. Since c is bound between $[0, 1]$, the local value does not need to be normalized first, as it can directly be multiplied by $(n_x - 1)$. σ_z^2 uses exponential spacing, but the correct index can be found in a similar way.

$$\begin{aligned} i_{\text{float}} &= (n_x - 1)\frac{x - x'[0]}{x'[n_x - 1] - x'[0]} \\ i &= 1 + \text{int}(i_{\text{float}}) \end{aligned} \tag{3.13}$$

$$f'_x = \frac{x - x'[i-1]}{x - x'[i-1]} \tag{3.14}$$

In cases where the local value is lower or higher than the minimum or maximum value used to construct the manifolds, the index is set to the lowest or highest point respectively. The interpolation factor is then determined for the local value compared to the neighbouring points. The interpolation factors are then used to perform the 4D interpolation. For each permutation of neighbouring points, the corresponding index in the manifold list is determined by means of Equation 3.15. Here, i, j, k, and l refer to the index of the control variable in their respective vector. The accent refers to whether the point is the lower or higher neighbour, with the value taking 0 or 1 respectively. Additionally, the interpolation factors for all control variables is combined into a single interpolation factor, using Equation 3.16. The contribution for each control variable in this equation is either f'_x if x' is 1, or $(1 - f'_x)$ if x' is 0.

$$i_{\text{Manifold}} = n_c \cdot n_{\sigma_c^2} \cdot n_{\sigma_z^2} \cdot (i - 1 + i') + n_{\sigma_c^2} \cdot n_{\sigma_z^2} \cdot (j - 1 + j') + n_{\sigma_c^2} \cdot (k - 1 + k') + (l - 1 + l') \tag{3.15}$$

$$\begin{aligned} f =& (1 - f'_z + i'(2f'_z - 1)) \cdot (1 - f'_c + j'(2f'_c - 1)) \\ & \cdot (1 - f'_{\sigma_z^2} + k'(2f'_{\sigma_z^2} - 1)) \cdot (1 - f'_{\sigma_c^2} + l'(2f'_{\sigma_c^2} - 1)) \end{aligned} \tag{3.16}$$

For each permutation of $[i', j', k', l']$, the entry in each manifold at $i_{\text{Manifold}} - 1$ is retrieved and multiplied by f. For each parameter, the sum of the resulting values is used as the interpolated value.

Control variable bounds

The progress variable is bound between 0 and 1. The mixture fraction is bound between 0.00891 and 0.17 for FGM A, 0.0074 and 0.00283 for FGMs B to E. The variances do not have a constant bound. Instead, their maximum values depend on the corresponding control variable, resulting in [0, c(1-c)] and [0, z(1-z)] respectively. The progress variable, mixture fraction and progress variable variance are uniformly spaced, the mixture fraction variance is exponentially spaced.

3.3.2. Boundary conditions

A number of different boundaries are determined. These are the inlet, bluff-body wall, inlet wall, plate wall and side outlet and upper outlet. In Table 3.2, the applied boundary conditions are shown. For parameters not stated in this table, no boundary conditions have been applied.

Boundary name	Inlet	Walls	Outlets
z [-]	Fixed value (0.0125)	Zero Gradient	Zero Gradient
c [-]	Fixed value (0)	Zero gradient	Zero gradient
$\sigma_{\tilde{z}}^2$ **[-]**	Fixed value (0)	Zero gradient	Zero gradient
$\sigma_{\tilde{c}}^2$ [-]	Fixed value (0)	Zero gradient	Zero gradient
h $[Jm^{-3}]$	Fixed value (-1.311)	Zero gradient	Zero gradient
ν_t	Zero gradient	Fixed value (1e-6)	No condition
p [Pa]	Zero gradient	Zero gradient	Fixed value (total pressure = 101325 Pa)
T [K]	Fixed value (298.15)	Zero gradient	Zero gradient
U $[ms^{-1}]$	Fixed mass flow rate (0.002287 kg/s)	No slip	Coupled to total pressure

Table 3.2: Numerical boundary conditions applied at domain edges, along with specified value where relevant.

4

Research Definition

4.1. Research Objective and Questions

As explained in the earlier sections, the need for less computationally intensive models for hydrogen combustion is clear. In general, if more phenomena are taken into account, the model and the required manifolds will be more complex. On the other hand, if less physics is taken into account, the accuracy and certainty of the model might be below the acceptable limit. The availability of accurate and computationally efficient models is beneficial for the design optimizations of hydrogen combustion systems.

The objective of this research is to improve hydrogen combustion modelling by determining the accuracy of lower fidelity models with regards to the behaviour of stretched premixed turbulent flames.

This leads to the following research question:

How do different Flamelet Generated Manifolds compare in accurately predicting the behaviour of strained hydrogen flames in Large Eddy Simulations?

This question is split into a number of sub-questions:

- Can FGM based models be used to model the interaction between strain rate and differential diffusion that is characteristic to strained hydrogen flames?
- How do the predicted spacial characteristics of the flame compare to higher fidelity models?
- How do the predicted conditional characteristics, such as local reaction rate, of the flame compare to higher fidelity models?

Main hypotheses

Since a significant part of the reacting zone will be in a region where stretch is expected, it is likely that the FGMs that incorporate stretch when building the databases will perform better than those that do not.

Furthermore, it is expected that non-unity Lewis number effects, such as differential diffusion, are predicted better by the FGMs that use a hydrogen based progress variable. Since these are phenomena caused by the hydrogen molecules, it is likely that using a progress variable based directly on their mass fraction leads to a better prediction of these phenomena than using H_2O as the progress variable. It is also expected that the FGM using a H_2O based progress variable will perform better in regions where the progress variable is higher.

Additionally, it is expected that the different models predict differences in the flame shape [22]. Since the flow field and chemistry both influence each other, it is likely that small differences in the conditional results can add up over the full domain, leading to more significant differences downstream. This will be stronger for models that do not capture the non-unity Lewis number effects sufficiently.

4.2. FGMs of interest

A number of different FGMs will be tested, which are described in Table 4.1. These are explained in further detail in subsection 3.2.4

FGM	progress variable	Strain rate [s^{-1}]
FGM A	c_{H_2O}	0
FGM B	c_{H_2}	0
FGM C	c_{H_2}	3000
FGM D	c_{H_2}	6000
FGM E	c_{H_2}	13000

Table 4.1: FGMs to be analyzed

4.3. Methodology & Test case

The FGMs will be studied by means of a test case using a bluff-body flow, which is explained in further detail in subsection 4.3.1. All simulations will start with the same initial conditions, determined using a lower fidelity model. The simulations are performed using the open source CFD software OpenFOAM, version 9. The simulations are performed on the national supercomputer Snellius, using 128 processor cores.

4.3.1. Test case

The simulation domain consists of an inlet, which leads to a larger cylindrical combustor. The inlet is restrained by a cylindrical rod, which is capped off by a conical bluff-body. The bluff-body causes a recirculation zone, which strains the flame. The test domain is illustrated in Figure 4.1. This domain corresponds with the experiment set-up used by Æsøy et al, [26]. The cone has an angle of 45°. The opening has a 3 mm gap. This leads to an opening surface area of 1.51e-4 m^2.

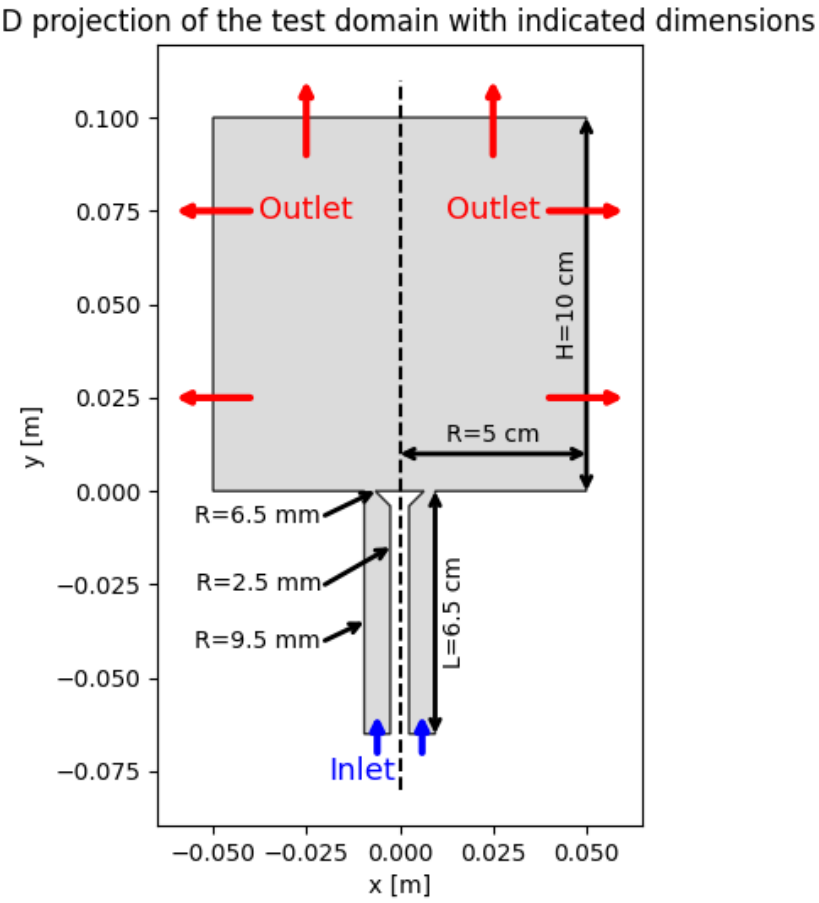

Figure 4.1: 2D projection of the test domain, showing the xy plane. Inlet is indicated in blue, outlets are indicated in red. The remaining boundaries are walls.

At the inlet, a mixture of hydrogen and air enters the system at a pressure of 1 atm and a temperature of 298 K. The equivalence ratio of the mixture is 0.4. The chemical power of the mixture is 3.5 kW, corresponding to a bulk mass flow of 0.002287 kg/s. The bulk velocity at the narrowest part of the bluff-body is 15.1 m/s. It takes a fluid particle 15 ms to travel through the domain. Each test will first allow complete flow-throughs through the system to allow for a quasi-steady state to be achieved. Then, the time-average is determined for the relevant parameters during another 4 flow-throughs. This leads to a total simulation time of 120 ms. The simulations use a constant time step of 1e-6 seconds.

5

Results

The results from the FGMs simulations are shown and compared to results determined by a higher fidelity Eulerian Stochastic Field (ESF) based model.

5.1. Comparison of temporal and spacial averages of results

To find the azimuthal averages of the relevant parameters in the combustor domain, the average is determined at 100 by 100 uniformly spaced radii and height levels. For each r and y, the value of the relevant parameters are assessed at 25 uniformly points along the circle determined by $r^2 = x^2 + z^2$, from which the average is taken as the azimuthal average for that (r, y). For the full domain, this is done for $0.1 \leq r \leq 49.5$ mm and $0.1 \leq y \leq 99.9$ mm. For close-ups of the attached part of the flame, $4.5 \leq r \leq 12.0$ mm and $0.1 \leq y \leq 30.0$ mm are used as limits. n_r, n_y and n_θ remain at 100 by 100 by .

5.1.1. Mixture fraction

In Figure 5.1, the azimuthal averages of the time-averaged mixture fraction in the combustor domain are shown. Figure 5.2 shows the same, but only the region surrounding the attached part of the flame. Especially in Figure 5.2, it can be seen that all models predict that the mixture fraction will first decrease below and then rise above the inlet mixture fraction value. This is typical for strained premixed hydrogen flames [14, 27]. This means that the FGMs are capable of at least qualitatively predicting the effect of strain on the mixture fraction changes due to differential diffusion.

The H_2 based FGMs predict a greater increase in mixture fraction at the flame front than both the ESF and FGM A. The latter predicts a slightly lower mixture fraction. The area containing the high mixture fraction is also larger for FGM B to E. This difference is visualized in the normalized difference plots shown in Figure 5.3 (full domain) and Figure 5.4 (close-up of attached flame). Figure 5.3 shows that there is a significant area downstream of the flame where FGM A predict a higher mixture fraction compared to FGMs B to E and the ESF. The latter FGMs do predict a lower mixture fraction along the center line of the domain, but these match the ESF better radially outward, with the exception of the dark blue region between $y = 16$ and $y = 33$ mm. The difference here is likely caused by a difference in vortex shedding.

All models predict a dip in mixture fraction, which can be most clearly seen in Figure 5.5. However, FGM A predicts this to a lesser degree than the ESF and the other FGMs. This can be explained by the fact that FGM A uses a H_2O based progress variable, whereas the other FGMs use H_2. Using H_2O as a progress variable means that effects at the start of the combustion process are not as well captured in the tabulation.

Except FGM E, all FGMs and the ESF predict a mixture fraction higher than the inlet mixture fraction directly in the wake of the bluff-body. Super-equilibrium conditions are expected in this region [14].

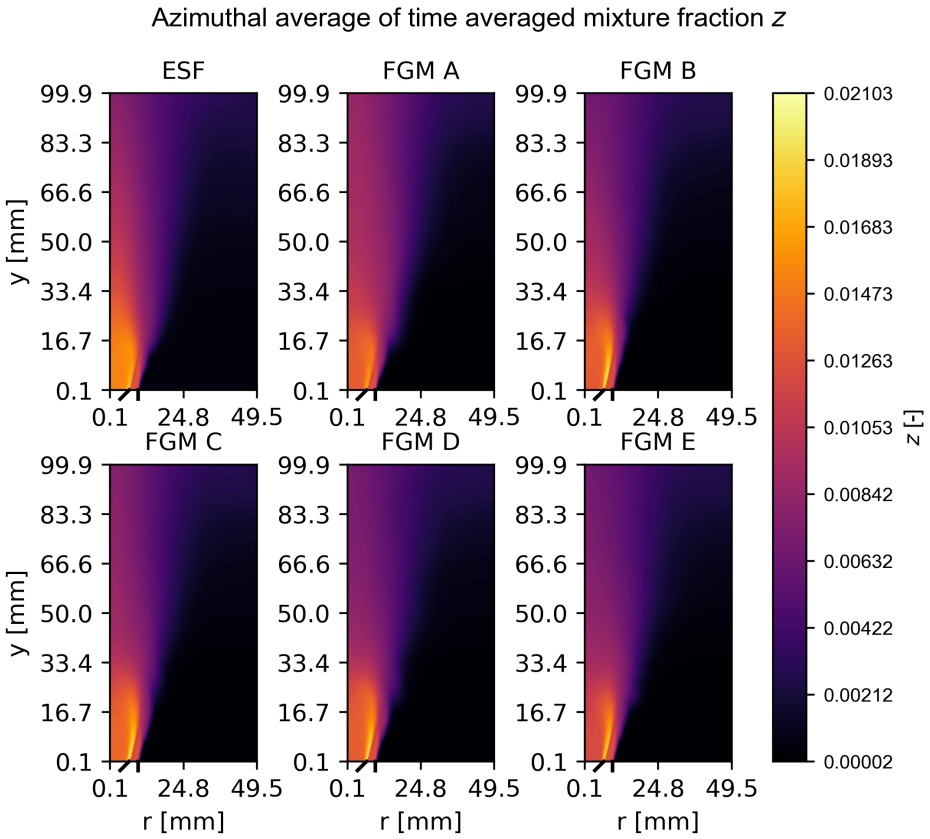

Figure 5.1: Plots showing the azimuthal average of the time average of the mixture fraction as determined by the ESF and FGMs models

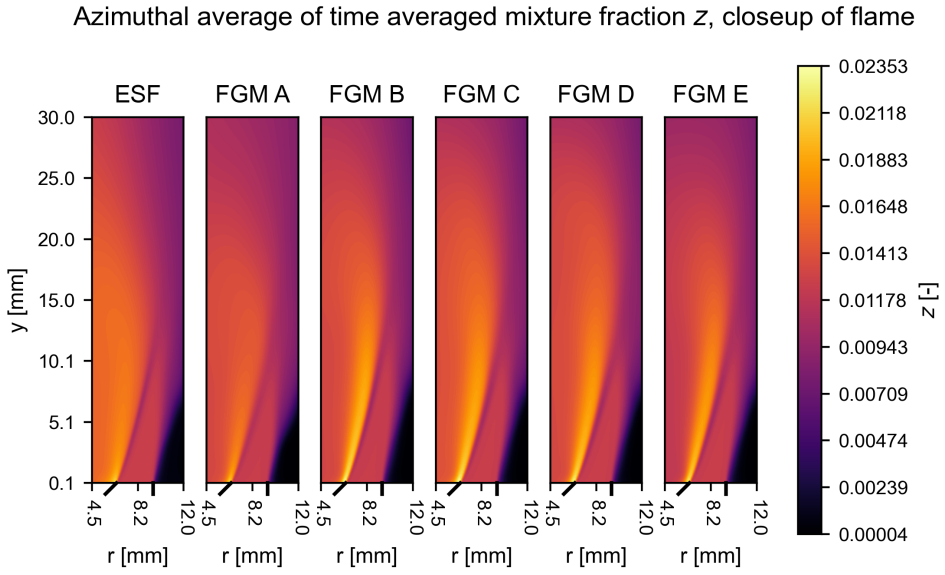

Figure 5.2: Plots showing the azimuthal average of the mixture fraction as determined by the ESF and FGMs models in the attached flame region

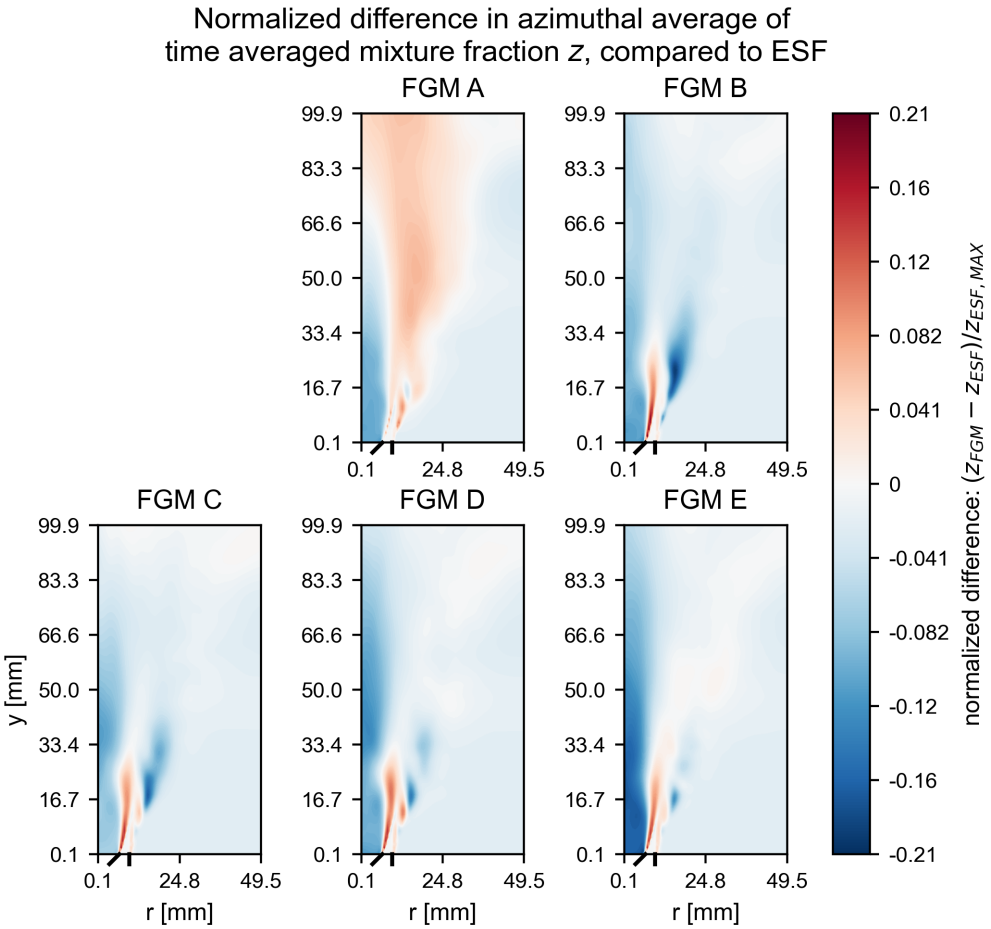

Figure 5.3: Normalized difference in azimuthal average of the time-averaged mixture fraction.

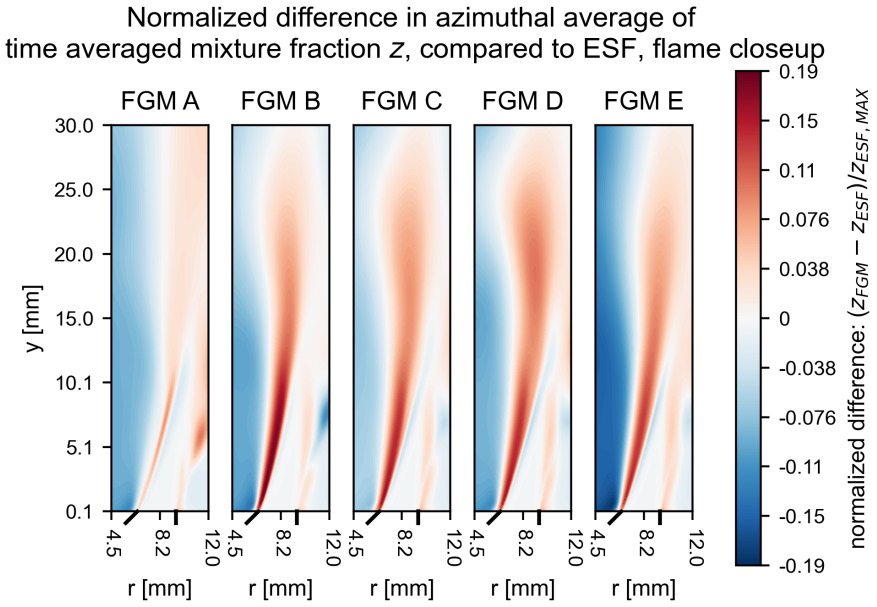

Figure 5.4: Normalized difference in azimuthal average of the time-averaged mixture fraction, close-up of the attached flame region.

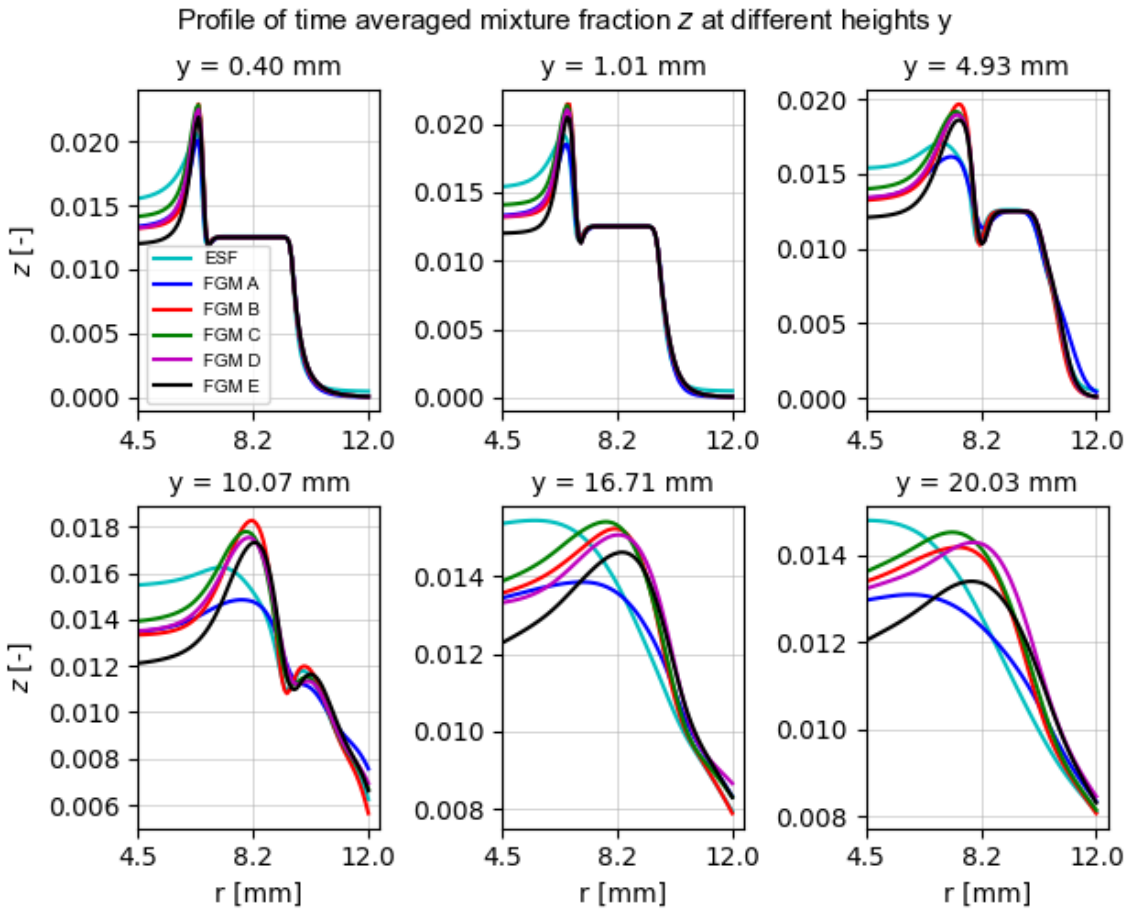

Figure 5.5: Profile of azimuthal average of time-averaged mixture fraction at various heights in the domain in the attached flame region.

5.1.2. Strain Rate

In Figure 5.6, the azimuthal average of the time averaged strain rate is shown. Figure 5.7 shows the normalized difference. The region of increased mixture fraction visible in Figure 5.2 on the inner side of the inlet jet coincides with the higher strain rate predicted in this region. This indicates that the FGMs are capable of at least qualitatively predicting the relationship between strain rate and mixture fraction seen in the ESF results and in other detailed chemistry models [27]. It should however be noted that near the flame front, all FGMs predict a higher strain rate than the ESF does.

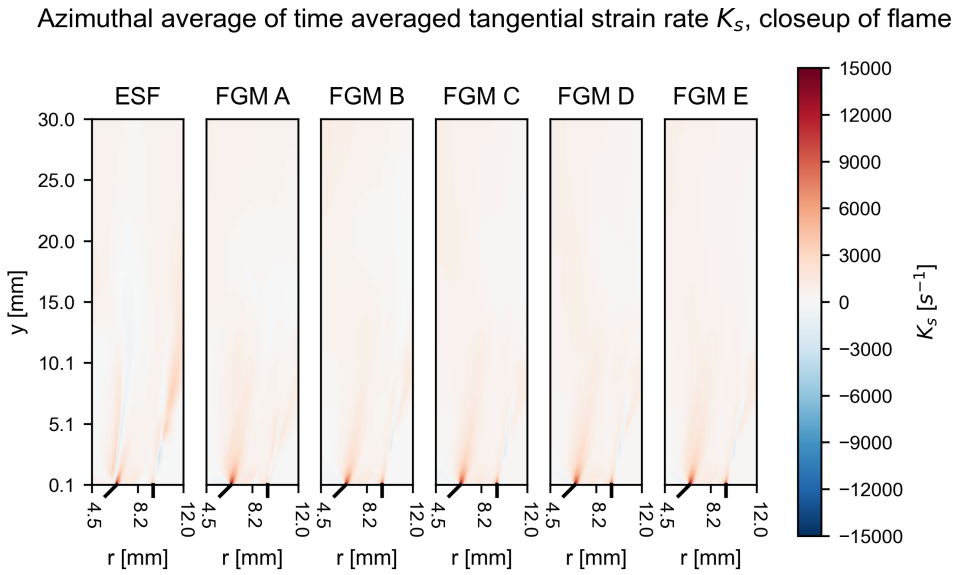

Figure 5.6: Plots showing the azimuthal average of the tangential strain rate as determined by the ESF and FGMs models in the attached flame region

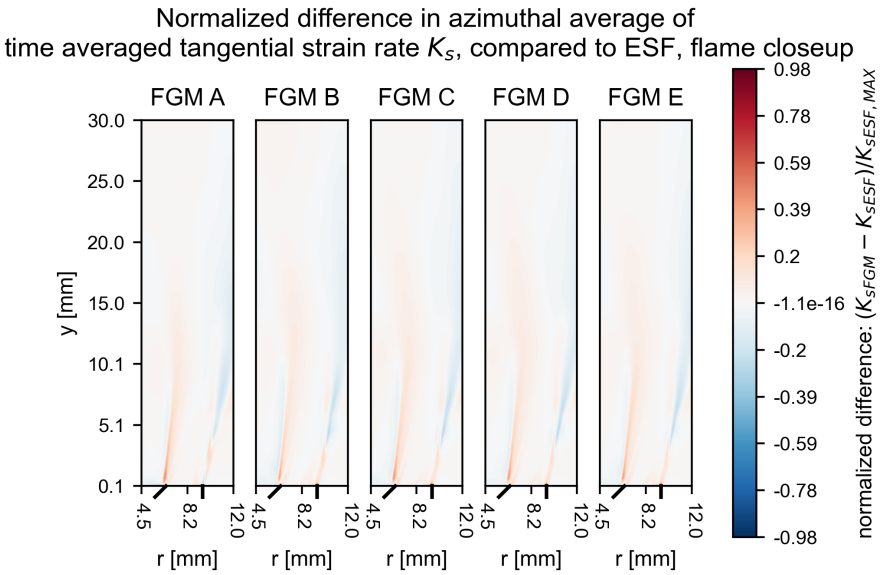

Figure 5.7: Plots showing the normalized difference in azimuthal average of the tangential strain rate as determined by the ESF and FGMs models in the attached flame region

5.1.3. Reaction rate

In Figure 5.8, the reaction rate as determined by the ESF and FGMs B to E is shown. FGM A is not included since it uses a different progress variable, so $\dot{\omega}_c$ is also different. In Figure 5.9, the normalized difference in $\dot{\omega}_c$ is shown. It can be seen FGM B initially under-predicts the reaction rate, but over-predicts the reaction rate higher in this region. For the FGMs uses strained flamelets, the difference can be explained by a slight change in the flame front location. Since the reaction zone is very thin, a small offset in radial direction can cause a large difference.

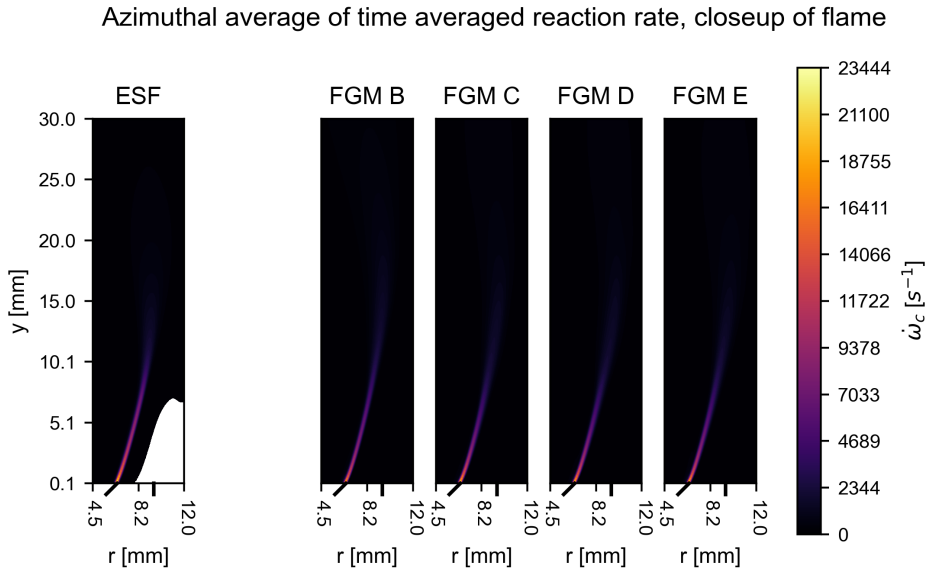

Figure 5.8: Plots showing the azimuthal average of the progress variable reaction rate as determined by the ESF and FGMs models. The black ticks on the x-axis represent the inlet geometry and location

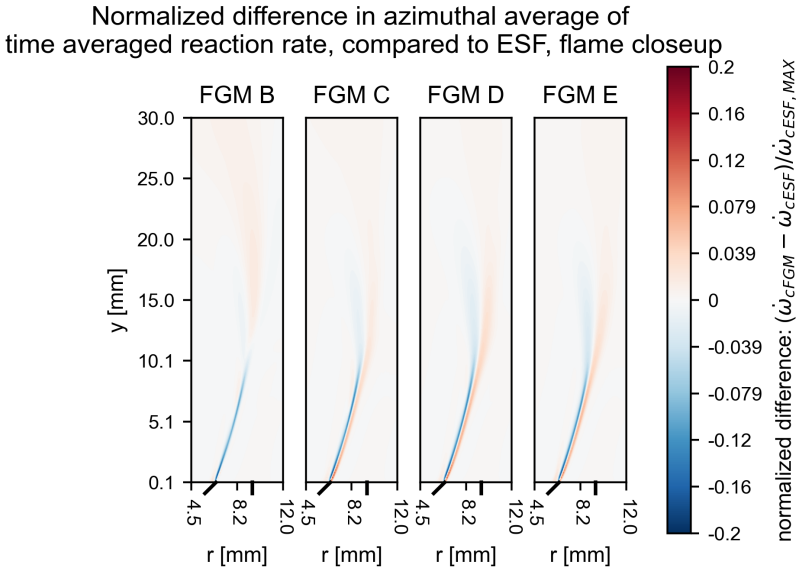

Figure 5.9: Plots showing the azimuthal average of the progress variable reaction rate as determined by the ESF and FGMs models. The black ticks on the x-axis represent the inlet geometry and location

In Figure 5.10, the profiles of the azimuthal average of $\dot{\omega}_c$ at different heights are shown. It can be seen that for y = 0.5, 1.9 and 4.9 mm, the FGMs predict a very similar peak reaction rate, which is lower than that of the ESF. The FGMs then predict a slower decrease in reaction rate as y increases compared to the ESF. This is especially true for the unstrained FGM B. This indicates that the model accuracy can be improved by carefully selecting a fixed strain rate for the flamelets.

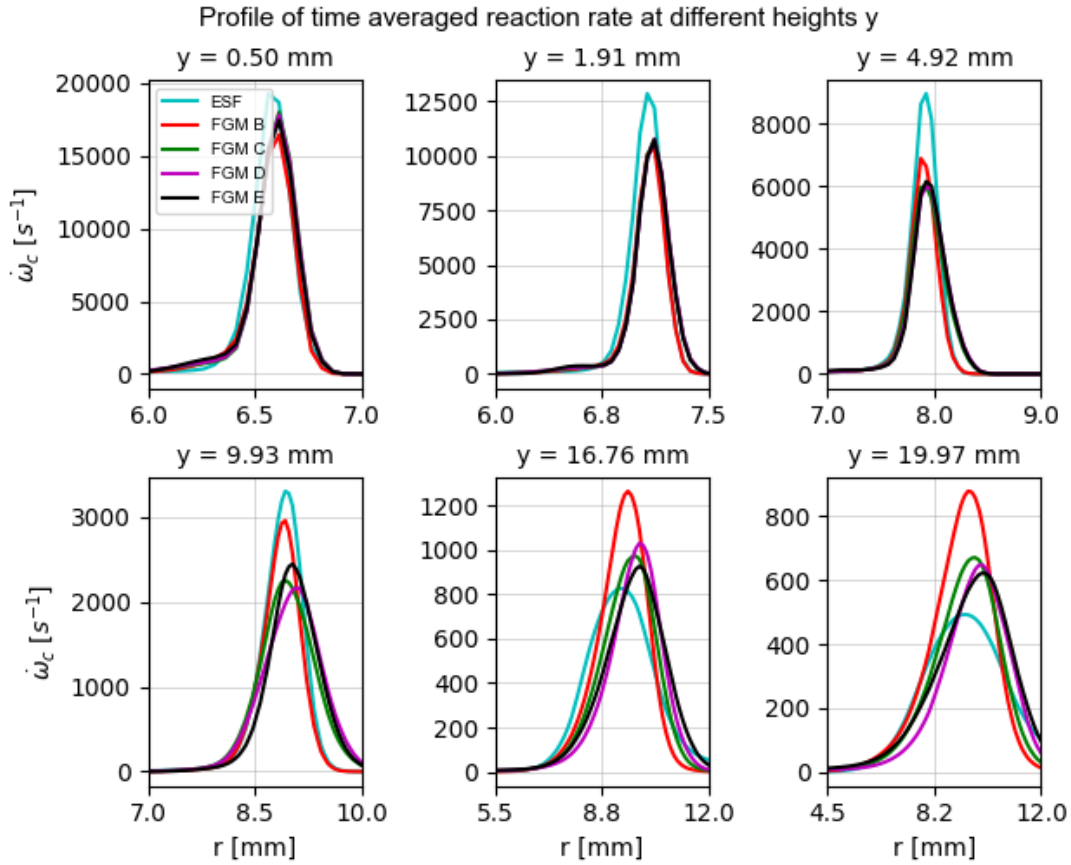

Figure 5.10: Profile of the azimuthal average of $\dot{\omega}_c$ at different heights in the attached flame

5.1.4. Temperature

In Figure 5.11, the azimuthal average of the temperature is shown. It can be seen that all H_2 based FGMs (FGMs B to E) have a narrower region of elevated temperature downstream in axial (y) direction of the flame compared to both the ESF and FGM A. The average temperature returns to the ambient temperature closer to the center line in the hydrogen based models.

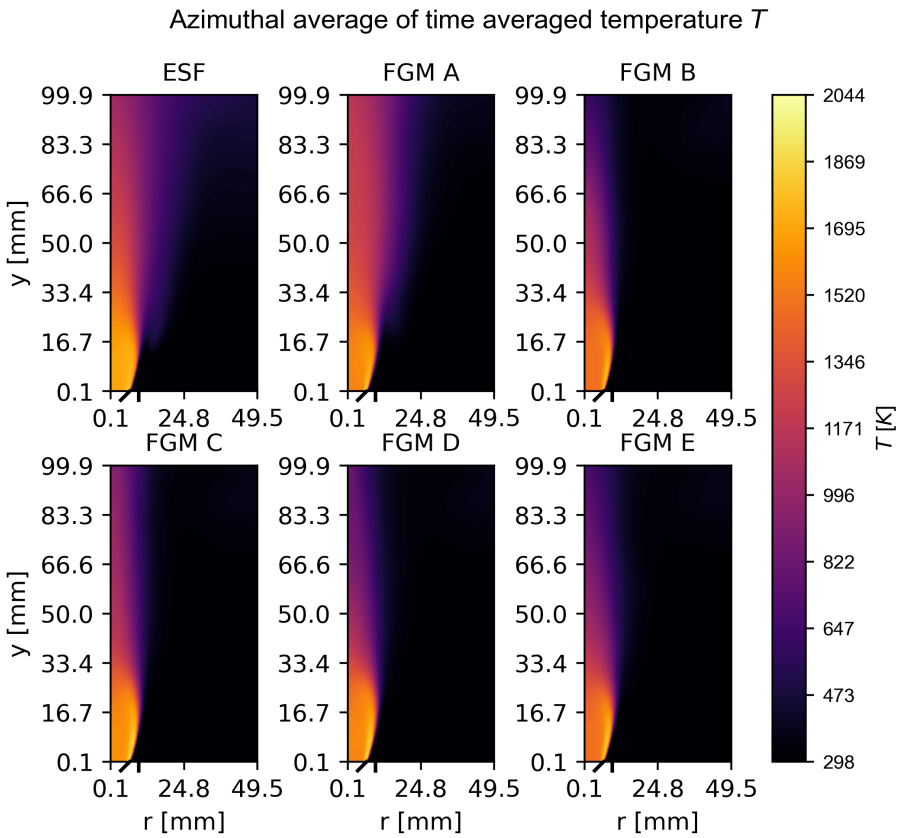

Figure 5.11: Plots showing the azimuthal average of the temperature as determined by the ESF and FGMs models. The black ticks on the x-axis represent the inlet geometry and location

In Figure 5.12, the normalized difference in temperature is shown. Here, it can be seen that all FGMs predict a higher temperature in the attached part of the flame. FGM A also predicts a higher temperature downstream of the flame, while the H_2 based FGMs predict a significantly lower temperature. A reason for the lower temperatures predicted by FGMs B to E could be that the tabulation for these FGMs is less suited in regions where the progress variable is high. These FGMs use a H_2 based progress variable. This causes to the tabulation to be less precise if the progress variable is high.

In the recirculation zone behind the bluff body, all FGMs predict a lower temperature compared to the ESF. This is similar to the mixture fraction prediction (Figure 5.3). The temperature in this region is still higher than the adiabatic flame temperature for an unstrained, 1-dimensional flame with an equivalence ratio of 0.4, which is expected [14]. In this region, FGMs C and D predicts temperatures closer to the ESf than the other H_2 based manifolds. This indicates that careful consideration of the flamelet strain rate can improve the temperature prediction somewhat.

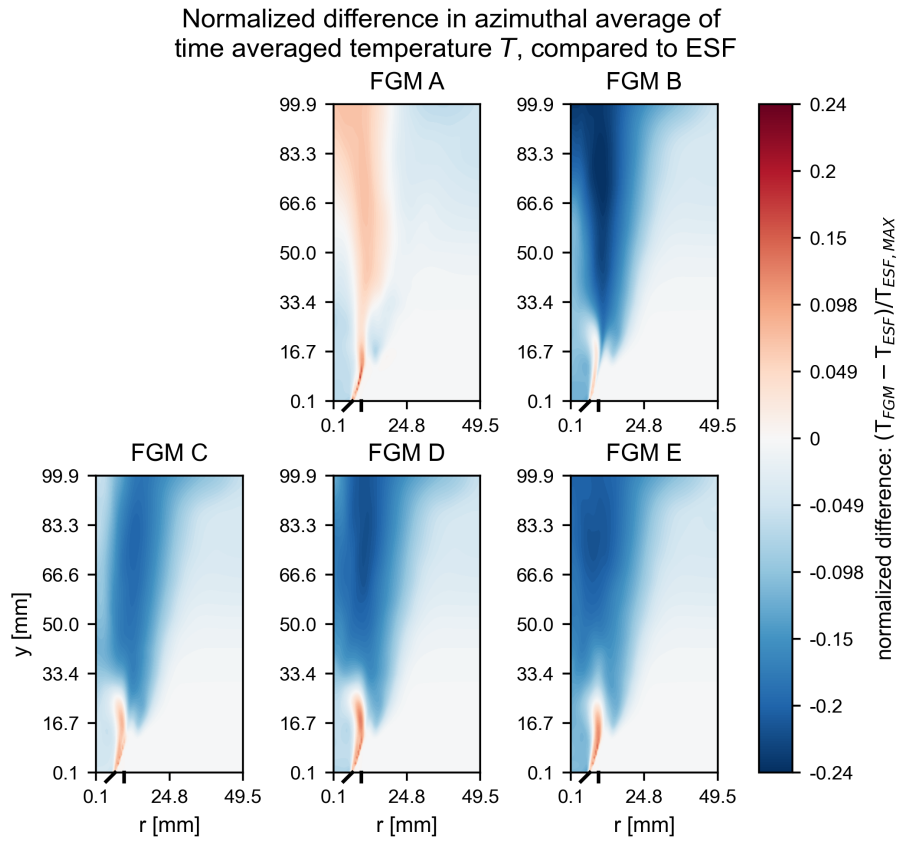

Figure 5.12: Normalized difference in azimuthal average of the time-averaged temperature. The black ticks on the x-axis represent the inlet geometry

In the profile plots shown in Figure 5.13 and Figure 5.16, the azimuthal average of the time averaged temperature at certain heights is shown, showing the entire domain and the attached flame region respectively. The profiles at y=0.4, 1 and 4.9 mm seen in Figure 5.16 show a higher peak temperature predicted by the FGMs. For the hydrogen based FGMs, this remains true at y = 10 mm. However, the FGMs predict a lower temperature than the ESF in the recirculation zone. This is is still a higher temperature than the adiabatic flame temperature of 1426 K. Super-adiabatic temperatures in the recirculation zone are expected [14]. The fact that the FGMs predict higher peak temperatures compared to the ESF at y=0.4, 1, 4.9 and 10 mm does not match the lower reaction rate shown in Figure 5.10. This suggests that other factors influence the temperature prediction, which should be investigated in future research.

In Figure 5.13, it can be seen that from y=33 mm onwards the H_2 based FGMs predict a significantly lower temperature than the ESF. FGM A tends to be significantly closer. FGM A predicts a slightly higher temperature radially inward ($r < 20$mm), and a lower temperature radially outward ($r > 20mm$ mm), while the hydrogen based FGMs predict a lower temperature. This can be explained by fact that the H_2O based FGM A is more refined for higher progress variable value, compared to the H_2 based FGMs.

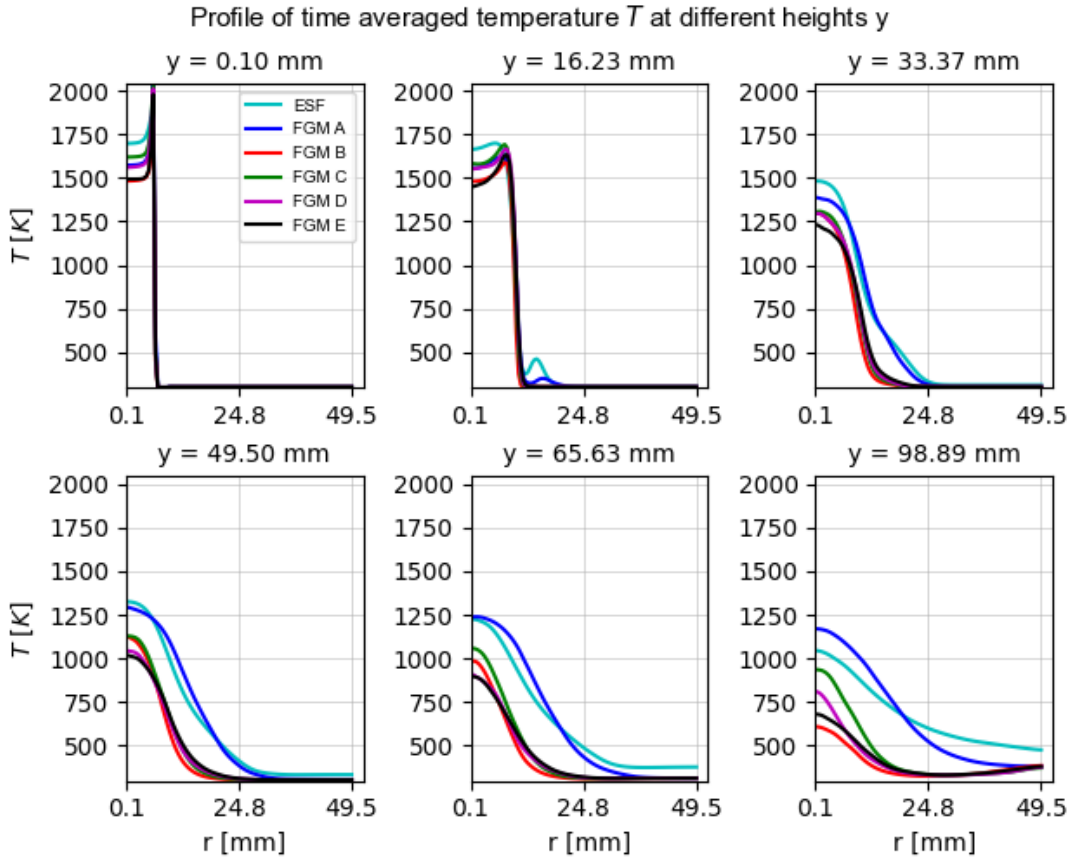

Figure 5.13: Profile of the azimuthal average of the temperature at different heights the domain

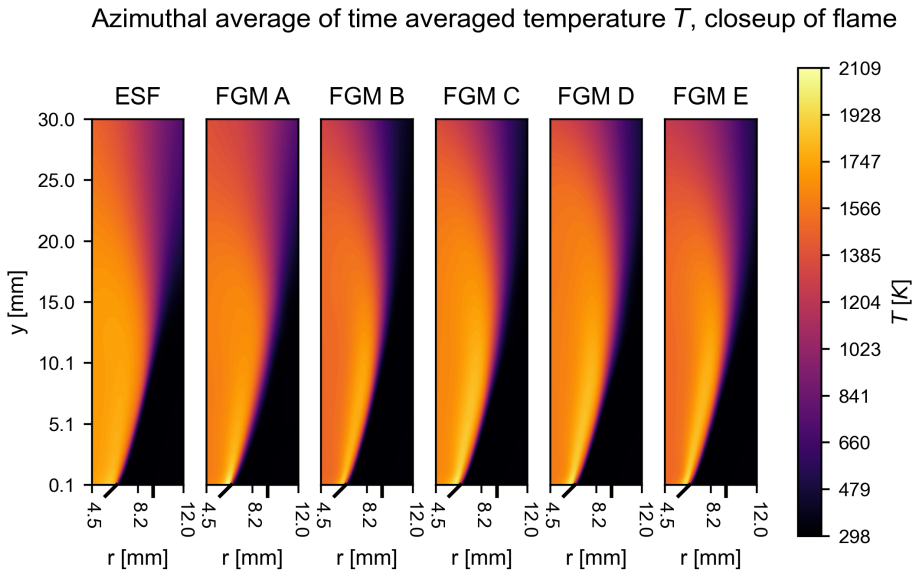

Figure 5.14: Plots showing the azimuthal average of the temperature as determined by the ESF and FGMs models in the attached flame region

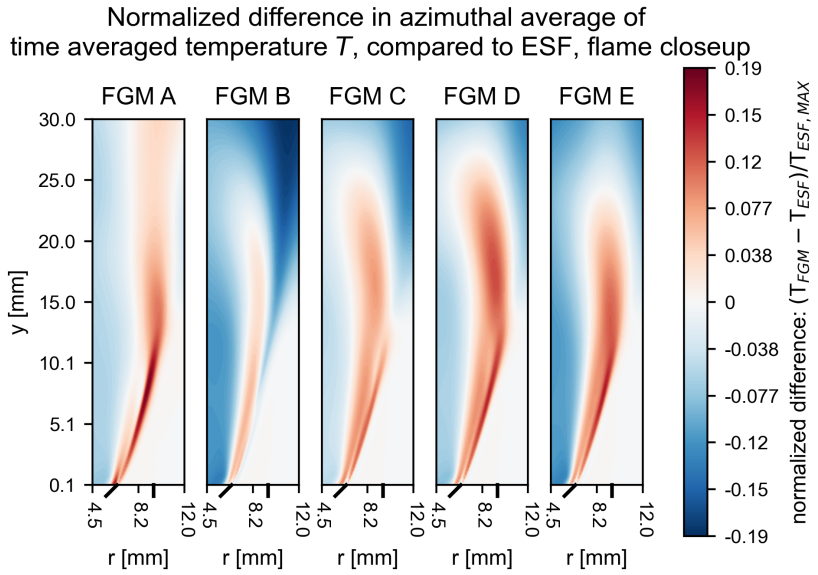

Figure 5.15: Normalized difference in azimuthal average of the time-averaged temperature in the attached part of the flame.

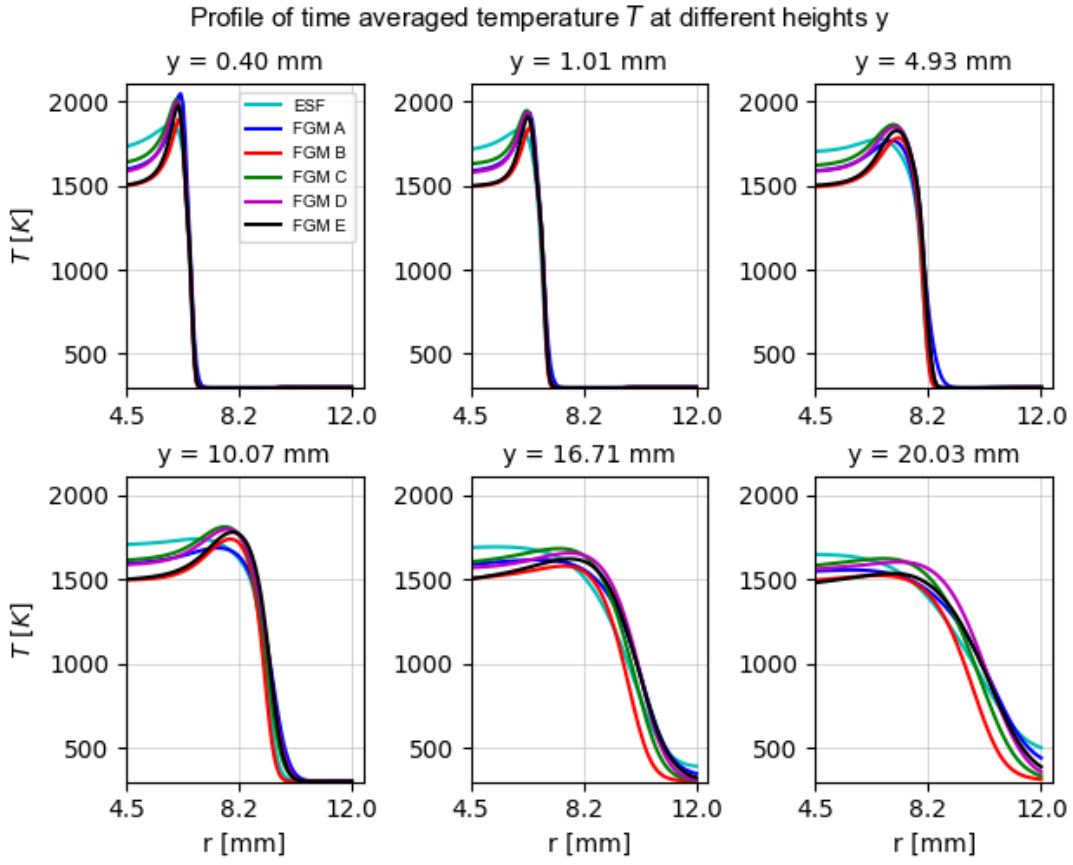

Figure 5.16: Profile of the azimuthal average of the temperature at different heights in the attached flame

5.1.5. Velocity

Magnitude

In Figure 5.17, the azimuthal average of the velocity magnitude is shown. It can be seen that FGMs B to E predict a lower velocity above y=33 mm. In Figure 5.18, the normalized difference is shown. Here, the lower velocity can clearly be seen. This also shows a significantly velocity predicted by the FGMs. This is especially true for the H_2 based FGMs. This difference is mainly caused by the fact that these FGMs predict a narrower inlet jet, as can be seen in Figure 5.19. In Figure 5.20, the normalized difference in time-averaged velocity is shown. It can also be seen that the FGMs predict a higher velocity in the inlet jet. The difference in flow features might be caused by local differences in reaction rate due to flame strain and differential diffusion. These differences can then in turn alter local flow features, which in turn alter the strain and thus reaction rate.

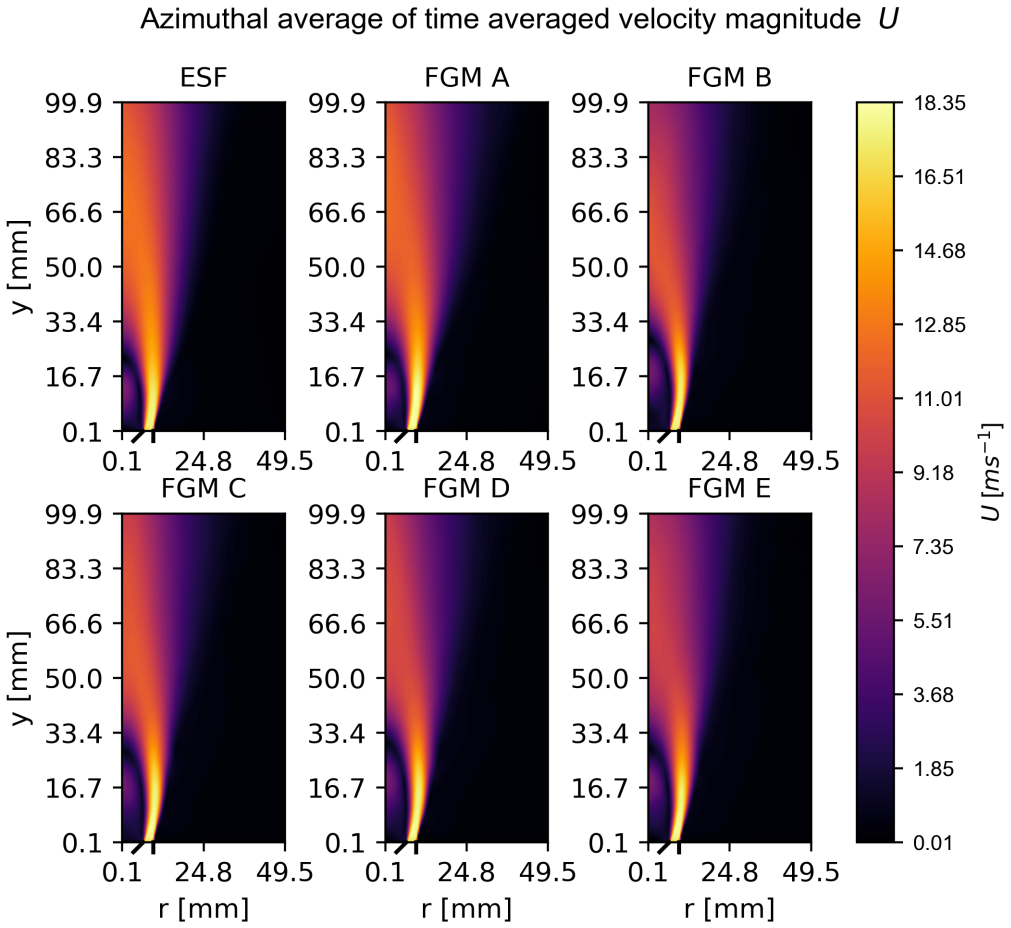

Figure 5.17: Plots showing the azimuthal average of the time-averaged velocity magnitude as determined by the FGMs and the ESF models

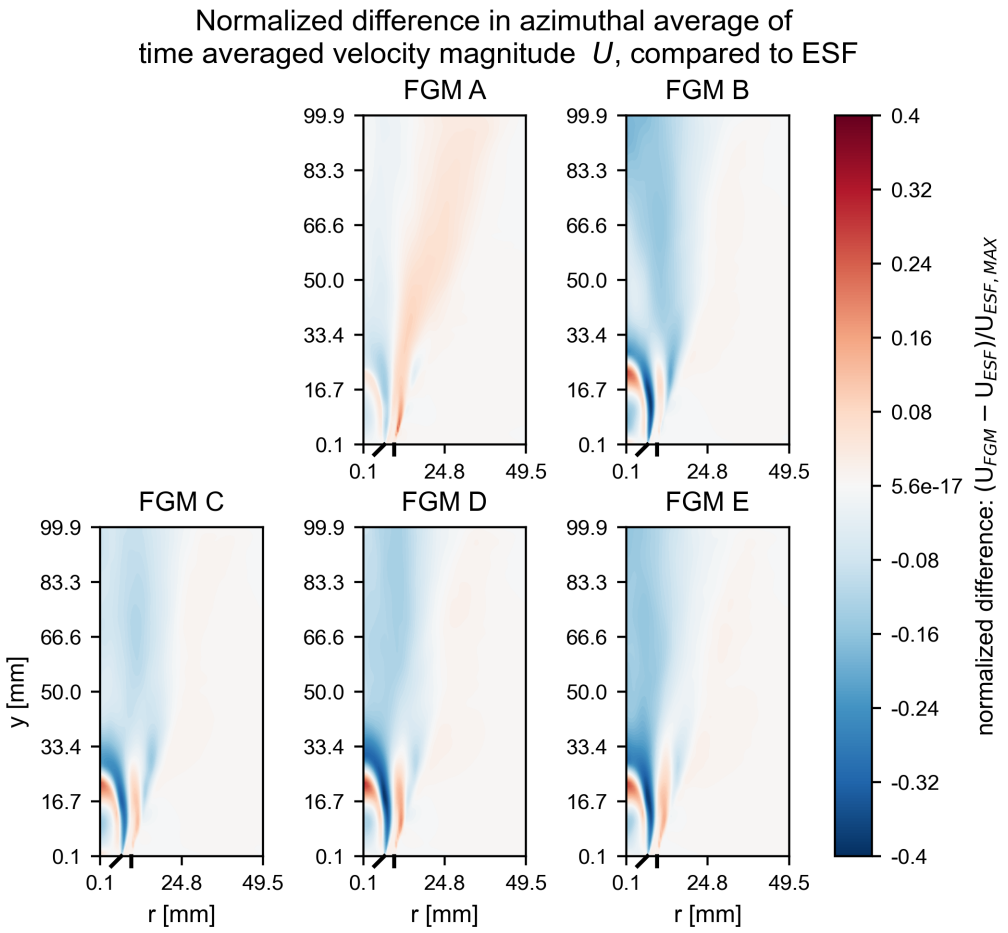

Figure 5.18: Plots showing the normalized difference in azimuthal average of the time-averaged velocity magnitude as determined by the FGMs and the ESF models

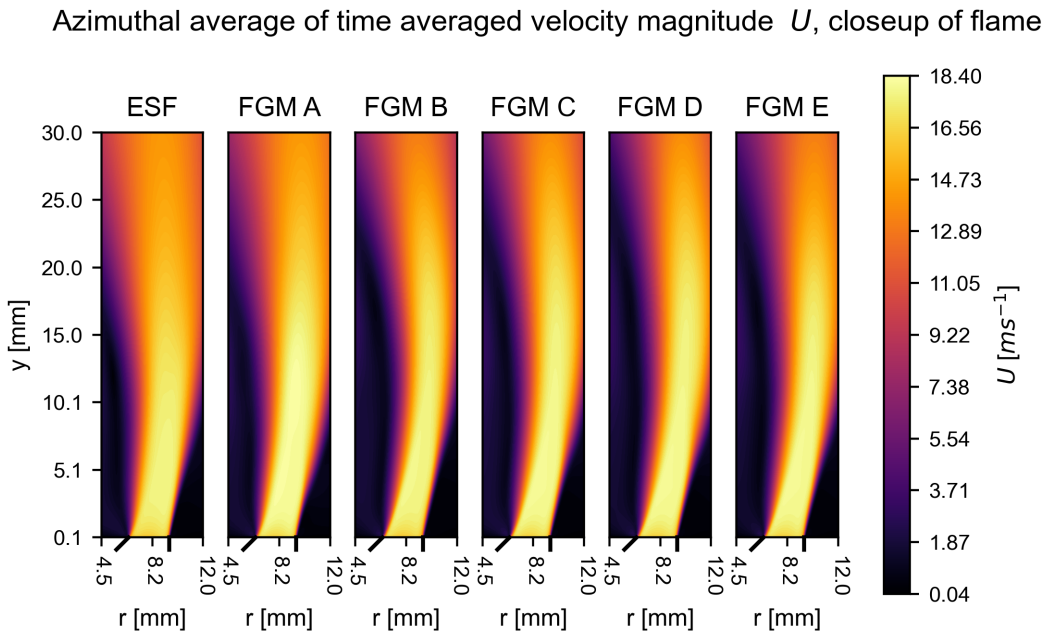

Figure 5.19: Plots showing the azimuthal average of the time-averaged velocity magnitude as determined by the FGMs and the ESF models in the attached flame

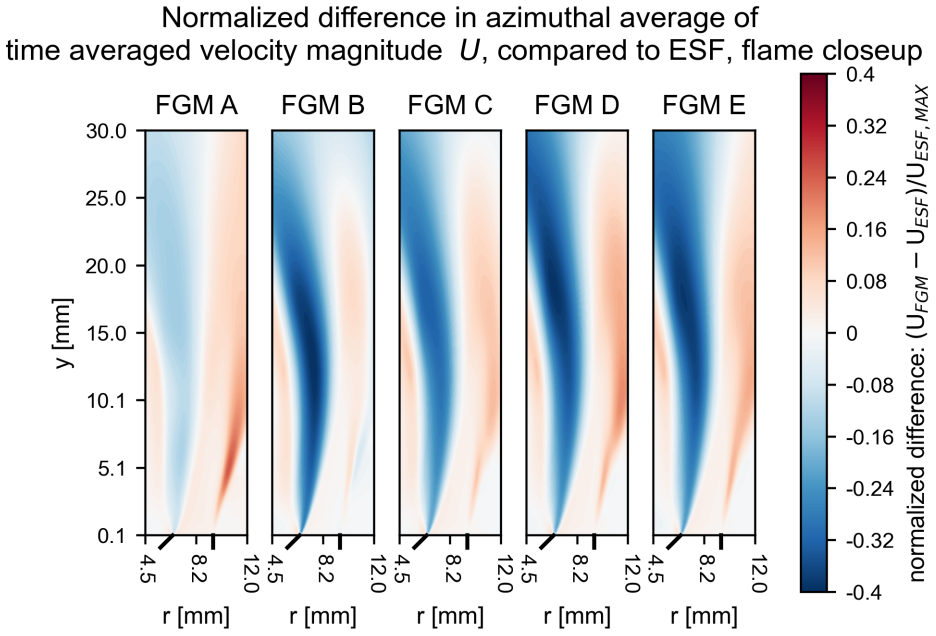

Figure 5.20: Plots showing the normalized difference in azimuthal average of the time-averaged velocity magnitude as determined by the FGMs and the ESF models in the attached flame

Axial velocity

In Figure 5.21, the axial velocity, i.e. the time average of the axial velocity (y-direction) is shown. In Figure 5.22, the normalized difference in this axial velocity is shown. In the recirculation zone directly behind the bluff-body, it can be seen that the FGMs predicts a longer region of downward flow compared to the ESF. This is especially true FGMs B to E. I.E., these FGMs predict a longer recirculation zone. Additionally, the downward flow in this region is less strong in the FGMs, as can be seen in Figure 5.22.

Above the recirculation zone, the FGMs predict a slower flow in axial direction compared to the FGMs. Only FGM A predicts a slightly faster flow upwards in regions away from the center line.

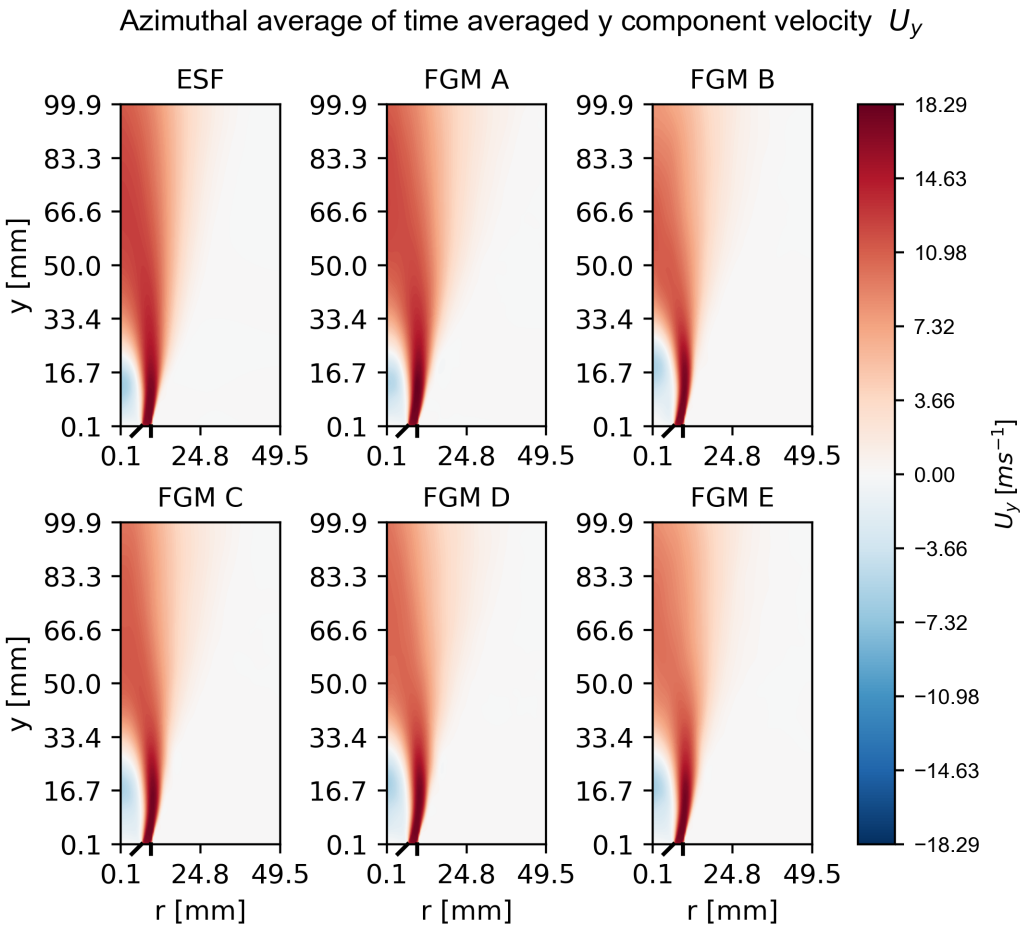

Figure 5.21: Plots showing the azimuthal average of the time-averaged axial velocity as determined by the FGMs and the ESF models

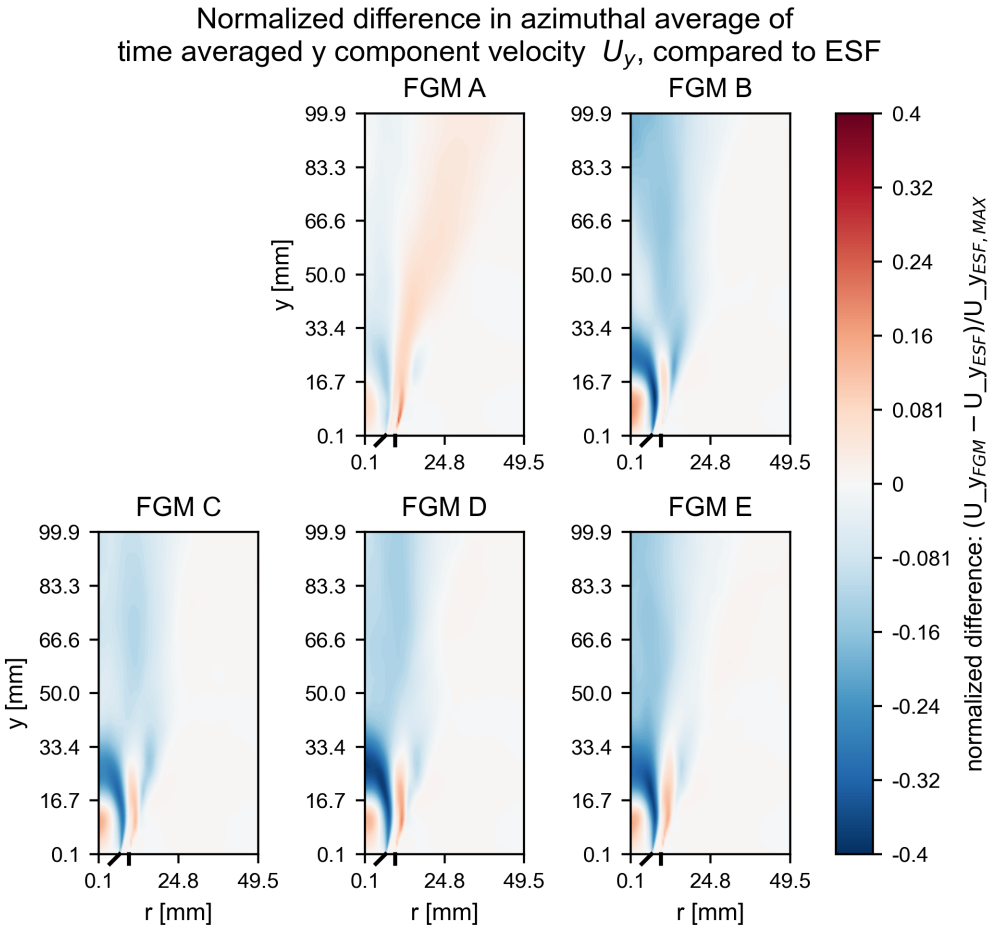

Figure 5.22: Plots showing the normalized difference in azimuthal average of the time-averaged axial velocity as determined by the FGMs and the ESF models

Radial Velocity

In Figure 5.23, the radial velocity is shown. Here, the longer recirculation zone can also be seen, as the radial velocity flips sign below y = 16.7 mm for the ESF and FGM A, but above y = 16.7 mm for FGMs B to E In Figure 5.24, the normalized difference in this radial velocity is shown. Additionally, the FGMs predict a slightly slower flow in the outgoing part in the recirculation zone.

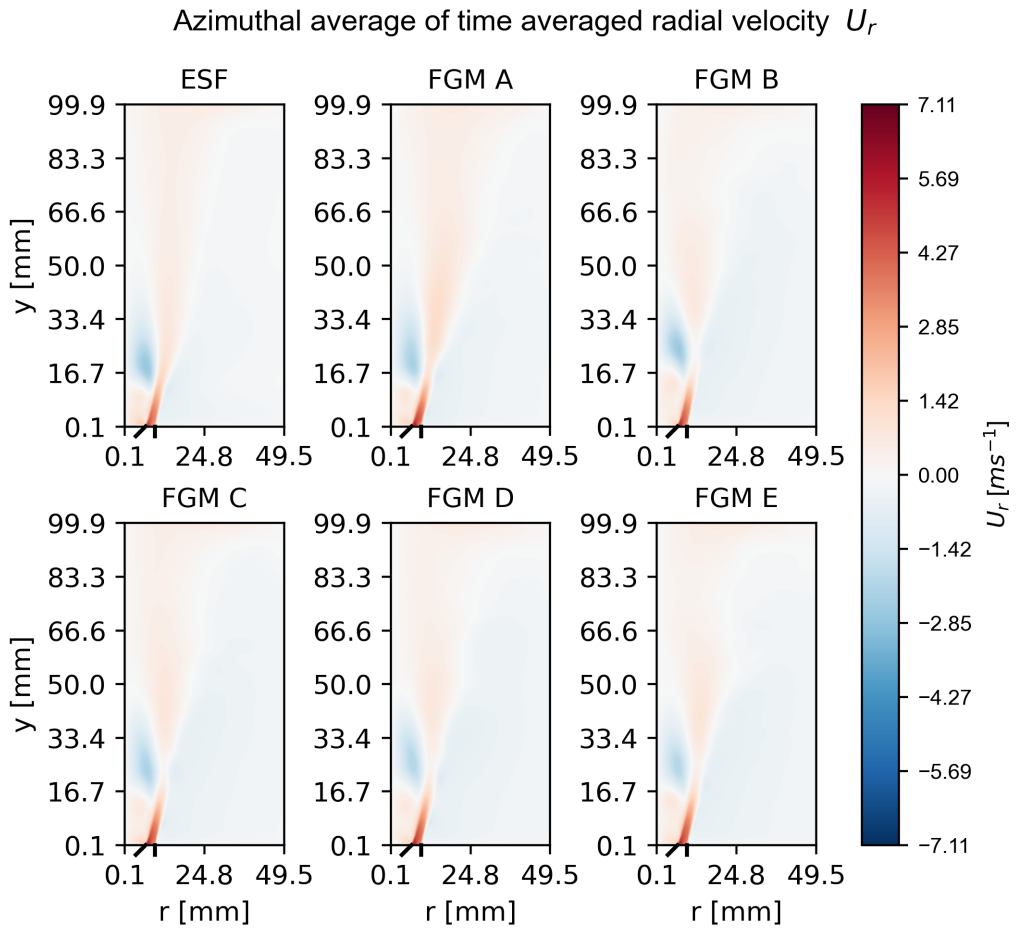

Figure 5.23: Plots showing the azimuthal average of the time-averaged radial velocity as determined by the FGMs and the ESF models

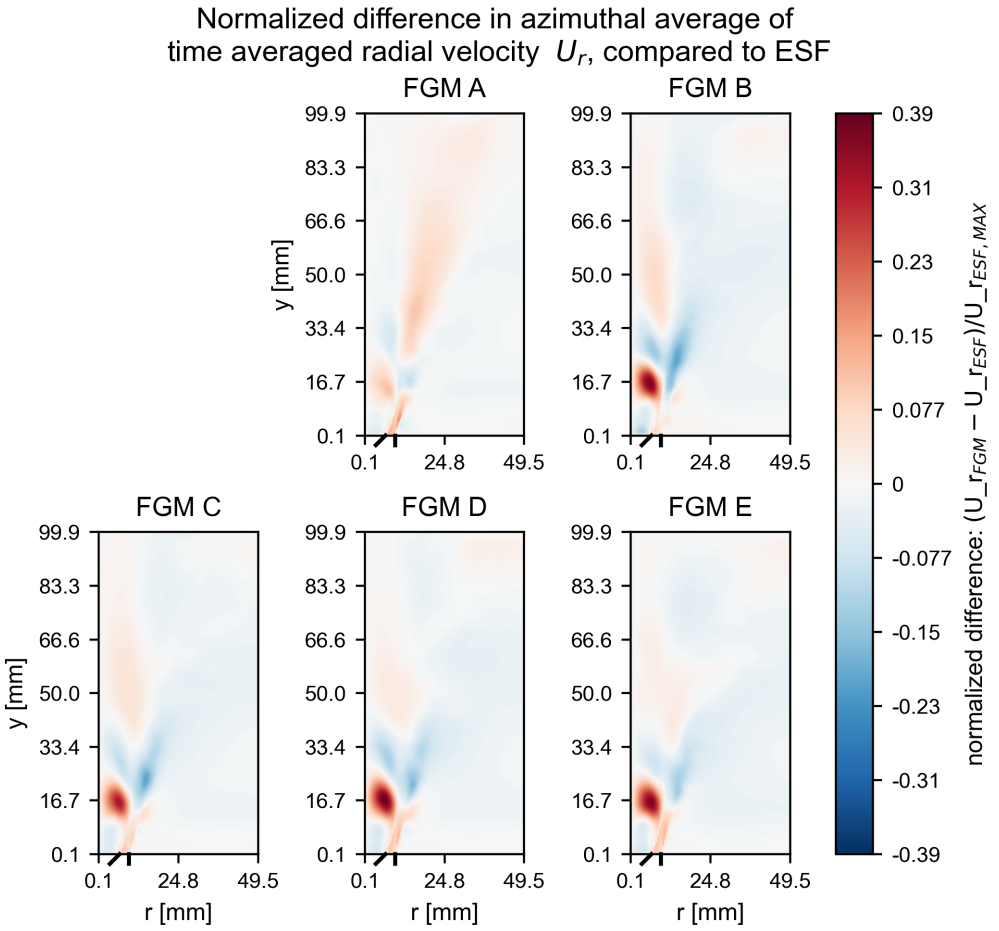

Figure 5.24: Plots showing the normalized difference in azimuthal average of the time-averaged radial velocity as determined by the FGMs and the ESF models

5.1.6. Interaction between strain and differential diffusion

The super-equilibrium conditions predicted by the models follow the interaction between strain rate and differential diffusion [14]. An increase in strain rate increases the local reactivity. This can influence the flow field, which can then in turn increase the strain rate, leading to more differential diffusion. One explanation for the higher peak mixture fraction and temperature predicted by the FGMs compared to the ESF could be that the FGMs over-predict the mutual effect between strain rate and differential diffusion.

5.1.7. Effect of shorter recirculation zone

Due to the interaction of strain and differential diffusion, super-equilibrium conditions can be observed [14]. These super-equilibrium products can then accumulate in the recirculation zone. Since the FGMs predicts a longer recirculation zone, the average strain rate of the surrounding flame front is lower. The super-equilibrium mixture fraction in this region is thus also lower on average, leading to a lower temperature and mixture fraction in the recirculation zone.

5.2. Conditionally averaged reaction rate

To quantitatively compare of the behaviour of the FGMs compared to the ESF, the conditionally averaged reaction rate is determined. This is done by determining the mean the progress variable source term $\dot{\omega}_c$ for each given c. Since the ESF model does not resolve a progress variable, c needs to be defined from the resolved mass fractions. For hydrogen, this is done using $c_{\mathrm{H_2}} = 1 - \frac{Y_{\mathrm{H_2}}}{Y_{\mathrm{H_2,max}}}$. $c_{\mathrm{H_2}}$ can then be used to compare the results from FGM B to E. The progress variable source term $\dot{\omega}_{c_{\mathrm{H_2}}}$ is then

defined as $\dot{\omega}_{c_{H_2}} = \frac{-\dot{\omega}_{H_2}}{\rho \max(Y_{H_2})}$. For FGM A, using the maximum mass fraction of H_2O is not a viable option due to the super-equilibrium conditions caused by differential diffusion in strained hydrogen flames. Therefore, the H_2O based progress variable has to be determined locally. This is done by using maximum mass fraction of H_2O for based on the height of each point. This approximation for c_{H_2O} is defines as $c_{H_2O} = \frac{Y_{H_2O}}{\max(Y_{H_2O}|y)}$. Just as with c_{H_2O}, a height-based maximum mass fraction is used to approximate $\dot{\omega}_{c_{H_2O}}$. It is defined as follows: $\dot{\omega}_{H_2O} = \frac{\dot{\omega}_{H_2O}}{\rho \max(Y_{H_2O}|y)}$. The density term in the denominator is needed to match the units of $\dot{\omega}_c$.

In Figure 5.25, the conditional mean of $\dot{\omega}_c$ as determined directly by the FGMs and of $\dot{\omega}_c$ determined by the post-processing of the ESF results is shown. It can be seen that the H_2 based FGMs (FGM B-E) show a better correspondence with the ESF results than the H_2O based FGM. This seemingly contradicts the results section 5.1, where FGM A shows a much better correspondence with the ESF results for temperature. The fact that the conditional means of the reaction rate predicted by the FGMs B to E match well with those predicted by the ESF show that the hydrogen based FGMs can predict the local reaction rates. However, the temperature prediction in these models can be improved. Predicting the temperature using FGMs adds an additional layer of uncertainty, as both the heat released and thermophysical characteristics of the fluid are retrieved from the FGM. FGM A works reasonably well in predicting both temperatures and reaction rates, although it does the latter worse than the other FGMs. It might be that some other effects compensate for the worse reaction rate prediction, leading to better temperature assessment. This should be further investigated. Furthermore, a better approximation for c_{H_2O} and $\dot{\omega}_{c_{H_2O}}$ in the ESF results could also be required.

FGM B also predicts a higher peak reaction rate than the ESF. Whilst the error can seemingly be reduced by using fixed-strain flamelets, this fixed strain should be carefully chosen. If the strain rate is too high, it leads to under-prediction, as can be seen in FGM E. Selecting the correct strain rate should be investigated in the future.

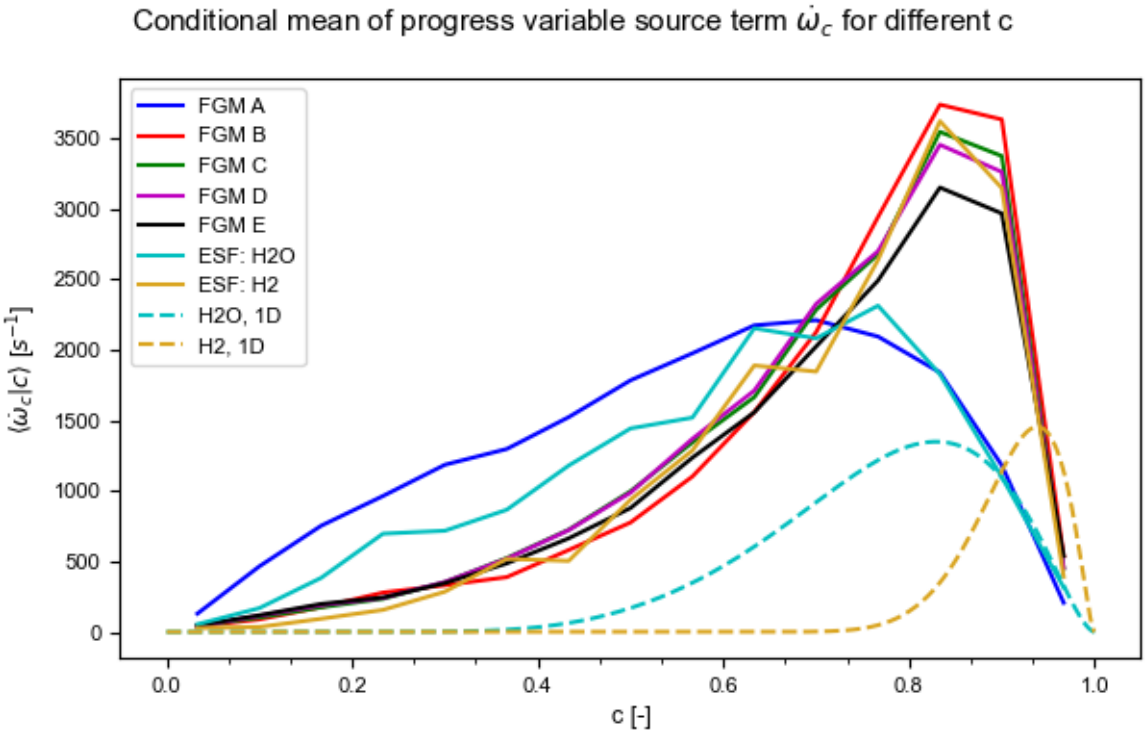

Figure 5.25: Plot of the conditional mean progress variable production rate $\dot{\omega}$ given a progress variable. The small tick markers in the x-axis show the bin edges. The dashed lines show the result for a unstrained, 1-dimensional simulation. To isolate the reacting region, only points where $\dot{\omega}_c \geq 1$ are taken into account.

It should also be noted that the progress variables for the ESF data has been determined after the simulations were completed, using the local mass fractions of the relevant species. This is not the same as actually solving for the progress variables during the run-time. While changes in local mass fraction could be due to the species being used or produced in reactions, changes can also occur due to diffusion. The effect of this is different for c_{H_2} and c_{H_2O}. For c_{H_2O}, differential diffusion causes the H_2O mass fraction to be higher than the equilibrium mass fraction in parts of the flame, and it causes the mass fraction to not be monotonic. This means that the maximum value of the mass fraction does not occur when the combustion is complete, but before this point is reached. The mass fraction then decreases as the combustion reaches completion. However, if the progress variable is then determined using the mass fraction, it is also non-monotonic, leading to the combustion process seemingly being reversed. Additionally, the combustion does not start at a constant mixture fraction. The mass fraction of H_2O at the end of combustion is dependent on the mixture fraction. This, in combination with the super-equilibrium mass fraction, makes using H_2O mass fraction to determine the progress variable in post-processing not possible.

For c_{H_2}, the local mass fraction can also change due to diffusion. Additionally, only using the mass fraction means that the progress variable for surrounding air is also 1, as the mass fraction of hydrogen there is 0. Whilst the surrounding air can be "filtered" from the results by setting a minimum threshold for $\dot{\omega}_c$ to find the actual reacting zone, the determined progress variable is still over-predicted in many regions, especially away from the attached part of the flame.

5.3. Parameter correlation comparison

To more reliably compare the different models, the normalized temperature ϕ_T is used. This is defined as $\phi_T = \frac{T-T_u}{T_{b,ad}-T_u}$, where T is the temperature and the subscripts u and b, ad represent the unburned and adiabatic flame temperature. The normalized temperature can also be viewed as type of progress variable. However, a drawback of using ϕ_T is that due to differential diffusion, the temperature does not monotonically increase as the combustion progresses. Additionally, super-adiabatic temperatures cause the normalized temperature to not be bounded to 1.

In Figure 5.26, a scatter plot showing the relation between the normalized temperature and mixture fraction is shown. To only include pairs from the reacting regions, only points where the threshold $\dot{\omega}_c > 1$ is met are included. For the ESF data, $\dot{\omega}_{c_{H_2}}$ is used, as defined in section 5.2.

For all FGMs, there are significantly less points at lower mixture fraction and ϕ_T compared to the ESF data. In Figure 5.27, the same pairing is shown, but now without a lower limit for $\dot{\omega}_c$. Here, the FGMs match the ESF significantly more closely. The likely explanation for this behaviour is that these points fall below the lowest value of the mixture fraction used in the manifolds. The model will then use the lowest value of the mixture fraction to determine the value of the tabulated parameters, as explained in subsection 3.3.1. Since the manifolds uses a mixture fraction higher than the actual mixture fraction for the interpolation, the tabulated parameters can not be accurately retrieved. This has no influence in the attached part of the flame, where most reactions occur. It can however influence regions where mixing with the ambient air occurs, as the mixture fraction is lower there. For this test-case for a lean and premixed flow, this drawback is not likely to be significant. However, it might be relevant non-premixed cases.

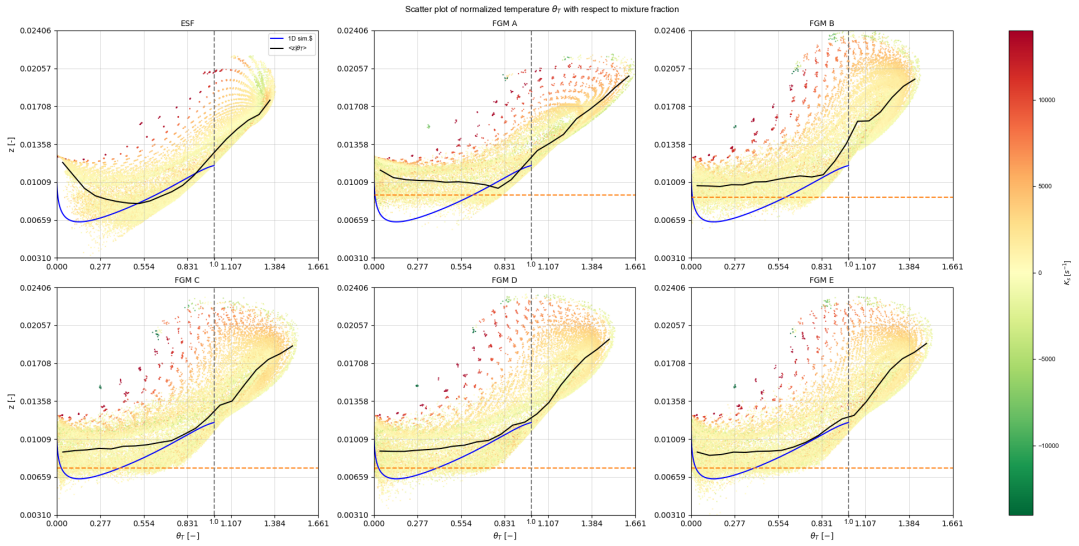

Figure 5.26: Scatter plot showing the relation between normalized temperature ϕ_T and mixture fraction z, coloured by tangential strain rate K_s. Only pairs where $\dot{\omega}_c > 1$ are included. The dashed orange line represents the minimum value of z used in the manifolds. The dashed gray line indicates $\phi_T = 1$. The solid black line represents the conditional average $< z|\phi_T >$. The solid blue line show the results from a 1-dimensional simulation.

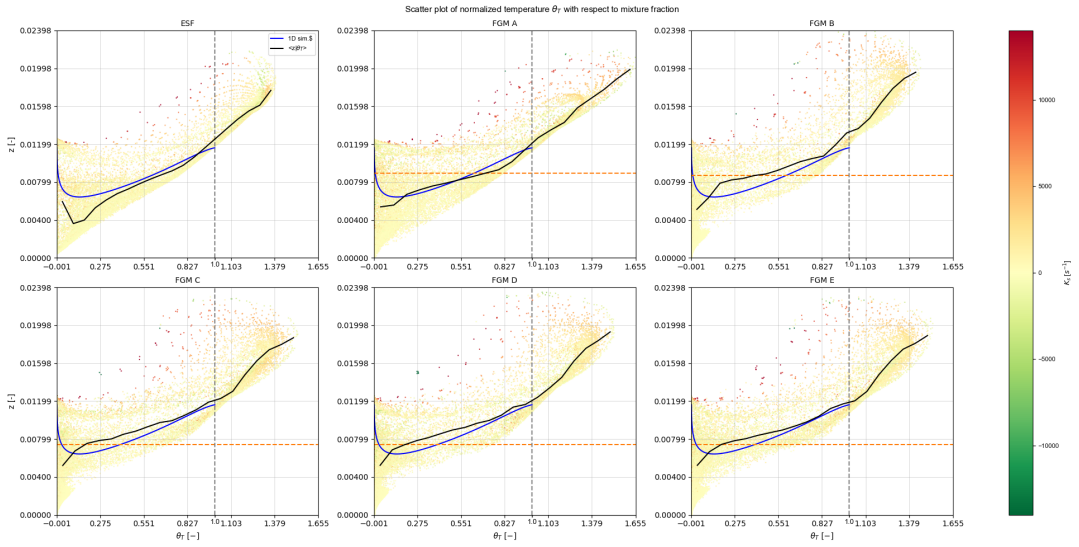

Figure 5.27: Scatter plot showing the relation between normalized temperature and mixture fraction, coloured by tangential strain rate. The dashed orange line represents the minimum value of z used in the manifolds. The dashed gray line indicates $\phi_T = 1$. The solid black line represents the conditional average $< z|\phi_T >$. The blue line show the results from a 1-dimensional simulation. No lower limit for $\dot{\omega}_c$ is applied here.

In Figure 5.28, a scatter plot showing the relationship between the mixture fraction and the tangential strain rate is shown. This shows that there is a wider range of strain rates predicted by the FGM based models, which matches the results shown in earlier sections. Additionally, for $z > 0.017$, the FGMs predicts that high z correlates with high strain rate. This is not the case in the ESF data. This indicates that the FGMs do indeed over-predict the mixture fraction increase due to the interaction between strain and differential diffusion.

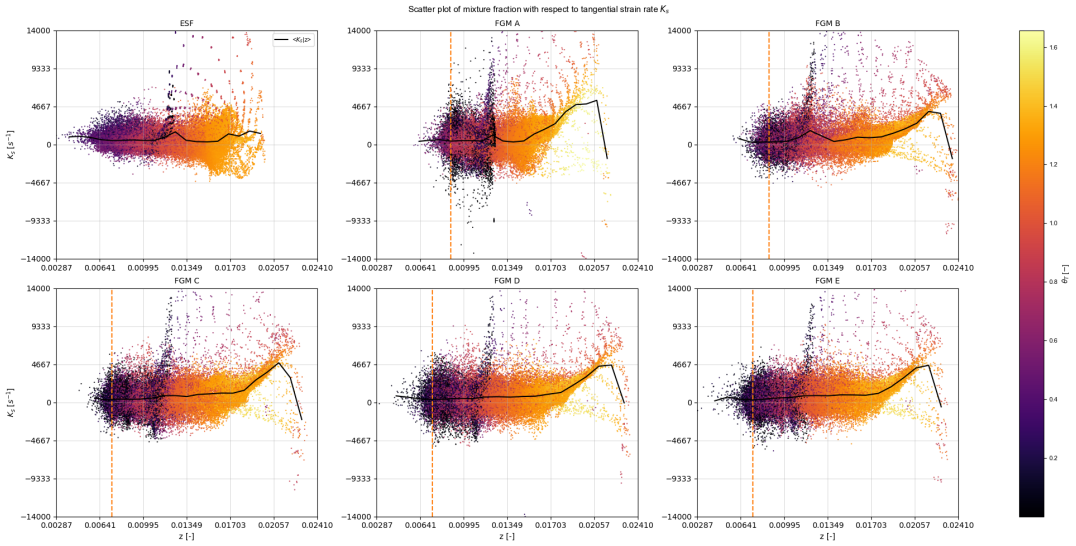

Figure 5.28: Scatter-plot showing the relation between mixture fraction and tangential strain rate, coloured by normalized temperature. Only pairs where $\dot{\omega}_c > 1$ are included. The orange dashed line indicates the minimum mixture fraction used for constructing the manifolds

In Figure 5.29, a scatter plot showing the relationship between z and curvature K_c is shown. The ESF shows that for mixture fractions above 0.015, there is correlation with higher mixture fraction and stronger negative curvature. FGMs A, C, D and E also predict this, but to a lesser degree. Additionally, as z then grows beyond $z = 0.017$, this correlation dissapears. Instead, higher mixture fraction can actually correlate with stronger positive curvature. This result indicates that the FGMs under-predict the relationship between negative curvature and differential diffusion.

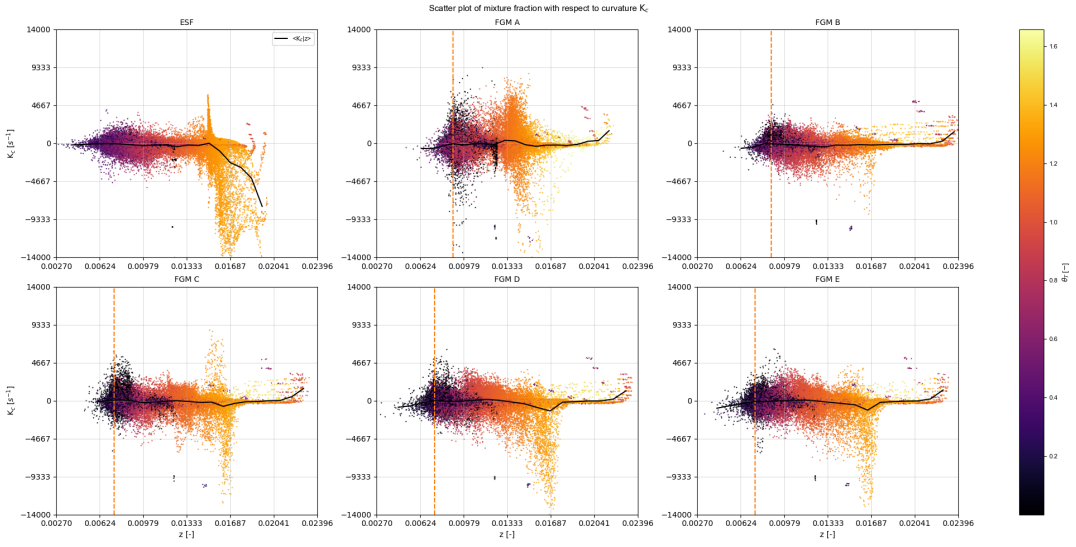

Figure 5.29: Scatter-plot showing the relation between mixture fraction and curvature, coloured by normalized temperature. Only pairs where $\dot{\omega}_c > 1$ are included. The orange dashed line indicates the minimum mixture fraction used for constructing the manifolds

6

Conclusions and Recommendations

The need for new energy carriers such as hydrogen is clear. However, a number of challenges need to be solved. One of these challenges is the fact that modelling hydrogen combustion is very computationally expensive due to a number of factors. By not solving the chemical reactions and chemistry-flow interaction directly, a significant decrease in computational cost can be achieved. By using a tabulated chemistry model combined with a statistics based approach for modelling sub-grid behaviour, a more reasonable computational cost can be achieved. In this paper, 5 different FGMs have been tested.

6.1. Main conclusions on obtained results

The results show that the FGMs based models are capable of predicting the existence of effects such as super-adiabatic temperatures and super-equilibrium products caused by differential diffusion. However, especially the hydrogen based FGMs predict a higher peak mixture fraction in the flame. This over-prediction is strongest for the unstrained FGM B, and decreases slightly with increase in flamelet strain rate. Since many characteristics such as heat release depend (partially) on the mixture fraction, a deviation in mixture fraction causes deviations in the temperature profile and behaviour of the mixture, which in turn has a large influence on the flow field. The change in the flow field then affects the reacting zone, causing a feedback loop.

All FGMs predict a different velocity profile compared to the ESF, resulting in a different shape of the recirculation zone. This effect is stronger in the H_2 based FGMs. The longer recirculation zone also influences the characteristics of the flow in the recirculation zone, leading to lower mixture fractions and temperature predicted by the FGMs. This is caused by the reduction in average differential diffusion of the surrounding flame, as the longer recirculation zone reaches regions with reduced strain rate. This can then in turn influence the reaction zone, leading to a feedback loop.

Locally, all FGMs give a good prediction of the conditionally averaged reaction rate $\langle \dot{\omega}_c | c \rangle$, and can therefore be used in a strained combustor setting with lean, premixed hydrogen. It should however be noted that there are still challenges, particularly with predicting the temperature. The hydrogen based FGMs struggle with this more, as these under-predict the temperature in regions outside of the flame front. The good prediction of $\dot{\omega}_c$ also happens despite the fact that the local effect of strain and differential diffusion are overestimated, and the interaction between negative curvature and differential diffusion are under-predicted.

There are regions where reactions might still occur, but where the mixture fraction is below the minimum mixture fraction used to construct the manifolds. While these regions are not significant in a lean premixed case, they could play a larger role in non-premixed cases.

6.2. Recommendations

In this work, only a single test scenario has been used. In order to validate the models for more general performance, more tests might be required. This could be done by varying the inlet velocity.

Additionally, this test has been performed using a pressure of 1 bar. To evaluate the performance of these FGM models in more practical applications for aerospace engineering, the model should ideally be tested under a wider range of initial and inlet conditions, such as a wider range of inlet temperatures and pressures to assess their performance.

Temperature prediction using FGMs brings an additional layer of uncertainty. Especially the hydrogen based FGMs under-predict the temperature in regions outside of the flame front. The cause of this should be investigated further.

No analysis has been done on the effect of changing the number of possible control variable states. An increase in the number of points in the manifold might lead to higher accuracy. In addition to this, no assessment is made on the spacing of the control variables. The results show that the hydrogen based FGMs tend to predict effects at lower c better, and vice versa for the water based FGM. This is likely caused by the fact that the progress variable is more refined at either the low or high end, respectively. Tuning the control variable spacing could be researched as a way of improving the accuracy of the models.

Additionally, for a given radius and height, the time-averaged results are not completely uniform for varying azimuthal angles. It might be that a longer simulation time could make the results more uniform. However, for the analysis performed in this research, taking the azimuthal average was deemed sufficient.

References

[1] United Nations. *Global Issues - Climate Change*. https://www.un.org/en/global-issues/climate-change. 2023.

[2] Intergovernmental Panel on Climate Change (IPCC). *Climate Change 2021 – The Physical Science Basis: Working Group I Contribution to the Sixth Assessment Report of the Intergovernmental Panel on Climate Change*. Cambridge University Press, 2023.

[3] Energy Institute. *Statistical Review of World Energy*. Tech. rep. Energy Institute, 2024.

[4] Karl W. Bandilla. "31 - Carbon Capture and Storage". In: *Future Energy (Third Edition)*. Ed. by Trevor M. Letcher. Third Edition. Elsevier, 2020, pp. 669–692. ISBN: 978-0-08-102886-5. DOI: https://doi.org/10.1016/B978-0-08-102886-5.00031-1. URL: https://www.sciencedirect.com/science/article/pii/B9780081028865000311.

[5] James G. Speight. "The Refinery of the Future (Second Edition)". In: ed. by James G. Speight. Gulf Professional Publishing, 2020. Chap. 12, pp. 427–468. ISBN: 978-0-12-816994-0. DOI: https://doi.org/10.1016/B978-0-12-816994-0.00012-9. URL: https://www.sciencedirect.com/science/article/pii/B9780128169940000129.

[6] James E. Funk. "Thermochemical hydrogen production: past and present". In: *International Journal of Hydrogen Energy* 26.3 (2001), pp. 185–190. ISSN: 0360-3199. DOI: https://doi.org/10.1016/S0360-3199(00)00062-8. URL: https://www.sciencedirect.com/science/article/pii/S0360319900000628.

[7] Goda Naujokaityté. *Hydrogen could be taken straight from the ground*. https://sciencebusiness.net/news/hydrogen-could-be-taken-straight-ground. Jan. 22.

[8] Department of State Office of the Historian. *Oil Embargo, 1973–1974*. Available at https://history.state.gov/milestones/1969-1976/oil-embargo. Archived on 1 October 2025, at https://web.archive.org/web/20251001192428/https://history.state.gov/milestones/1969-1976/oil-embargo. 2025.

[9] Heinz Pitsch. "The transition to sustainable combustion: Hydrogen- and carbon-based future fuels and methods for dealing with their challenges". In: *Proceedings of the Combustion Institute* 40.1 (2024), p. 105638. ISSN: 1540-7489. DOI: https://doi.org/10.1016/j.proci.2024.105638. URL: https://www.sciencedirect.com/science/article/pii/S1540748924004462.

[10] Rui Zhang et al. "Gaseous hydrogen permeation of pipeline steels: A focused review". In: *Renewable and Sustainable Energy Reviews* 211 (2025), p. 115304. ISSN: 1364-0321. DOI: https://doi.org/10.1016/j.rser.2024.115304. URL: https://www.sciencedirect.com/science/article/pii/S136403212401030X.

[11] Qian Zhao et al. "Study on hydrogen embrittlement behaviour of X52 welded joints in hydrogen transport environments". In: *Engineering Failure Analysis* 179 (2025), p. 109774. ISSN: 1350-6307. DOI: https://doi.org/10.1016/j.engfailanal.2025.109774. URL: https://www.sciencedirect.com/science/article/pii/S1350630725005151.

[12] Ibrahim Dincer. "Technical, environmental and exergetic aspects of hydrogen energy systems". In: *International Journal of Hydrogen Energy* 27.3 (2002), pp. 265–285. ISSN: 0360-3199. DOI: https://doi.org/10.1016/S0360-3199(01)00119-7. URL: https://www.sciencedirect.com/science/article/pii/S0360319901001197.

[13] Pieter-Jan Proesmans and Roelof Vos. "Comparison of Future Aviation Fuels to Minimize the Climate Impact of Commercial Aircraft". In: *AIAA AVIATION 2022 Forum* (June 2022). DOI: 10.2514/6.2022-3288. URL: https://arc.aiaa.org/doi/abs/10.2514/6.2022-3288.

[14] Lukas Berger, Antonio Attili, and Heinz Pitsch. "Synergistic interactions of thermodiffusive instabilities and turbulence in lean hydrogen flames". In: *Combustion and Flame* 244 (2022), p. 112254. ISSN: 0010-2180. DOI: https://doi.org/10.1016/j.combustflame.2022.112254. URL: https://www.sciencedirect.com/science/article/pii/S0010218022002693.

[15] Sara Sami Taha et al. "Comprehensive review of health impacts of the exposure to nitrogen oxides (NOx), carbon dioxide (CO2), and particulate matter (PM)". In: *Journal of Hazardous Materials Advances* 19 (2025), p. 100771. ISSN: 2772-4166. DOI: https://doi.org/10.1016/j.hazadv.2025.100771. URL: https://www.sciencedirect.com/science/article/pii/S2772416625001822.

[16] Gerhard Lammel and Hartmut Graßl. "Greenhouse Effect of NOx". In: *Environmental Science and Pollution Research* 2 (1995), pp. 40–45. DOI: https://doi.org/10.1007/BF02987512. URL: https://link.springer.com/article/10.1007/BF02987512.

[17] George A. Lavoie, John B. Heywood, and James C. Keck. "Experimental and Theoretical Study of Nitric Oxide Formation in Internal Combustion Engines". In: *Combustion Science and Technology* 1.4 (1970), pp. 313–326. DOI: https://doi.org/10.1080/00102206908952211. URL: https://doi.org/10.1080/00102206908952211.

[18] S. Taamallah et al. "Fuel flexibility, stability and emissions in premixed hydrogen-rich gas turbine combustion: Technology, fundamentals, and numerical simulations". In: *Applied Energy* 154 (2015), pp. 1020–1047. ISSN: 0306-2619. DOI: https://doi.org/10.1016/j.apenergy.2015.04.044. URL: https://www.sciencedirect.com/science/article/pii/S0306261915004997.

[19] Alexander Starik et al. "Syngas Oxidation Mechanism". In: *Combustion Explosion and Shock Waves* 46 (Sept. 2010), pp. 491–506. DOI: 10.1007/s10573-010-0065-x.

[20] J.K. Bechtold and M. Matalon. "The dependence of the Markstein length on stoichiometry". In: *Combustion and Flame* 127.1 (2001), pp. 1906–1913. ISSN: 0010-2180. DOI: https://doi.org/10.1016/S0010-2180(01)00297-8. URL: https://www.sciencedirect.com/science/article/pii/S0010218001002978.

[21] Michael P. Burke et al. "Comprehensive H2/O2 kinetic model for high-pressure combustion". In: *International Journal of Chemical Kinetics* 44.7 (June 2011), pp. 444–474. DOI: https://doi.org/10.1002/kin.20603. URL: https://onlinelibrary.wiley.com/doi/abs/10.1002/kin.20603.

[22] Gioele Ferrante, Georg Eitelberg, and Ivan Langella. "Differential diffusion modelling for LES of premixed and partially premixed flames with presumed FDF". In: *Combustion Theory and Modelling* 28.6 (2024), pp. 695–730. DOI: 10.1080/13647830.2024.2389099. URL: https://doi.org/10.1080/13647830.2024.2389099.

[23] Paola Breda et al. "Validation of an Eulerian Stochastic Fields Solver Coupled with Reaction–Diffusion Manifolds on LES of Methane/Air Non-premixed Flames". In: *Flow, Turbulence and Combustion* (Aug. 2021), pp. 441–477. ISSN: 1573-1987. DOI: 10.1007/s10494-020-00235-w. URL: https://link.springer.com/article/10.1007/s10494-020-00235-w.

[24] Lukas Berger et al. "LES combustion model for premixed turbulent hydrogen flames with thermodiffusive instabilities: a priori and a posteriori analysis". In: *Journal of Fluid Mechanics* 1003 (2025), A33. DOI: 10.1017/jfm.2024.1201.

[25] G. Rocco et al. "Curvature Effects in Turbulent Premixed Flames of H2/Air: a DNS Study with Reduced Chemistry". In: *Flow, Turbulence and Combustion* 94 (2015), pp. 359–379. DOI: https://doi.org/10.1007/s10494-014-9576-y. URL: https://link.springer.com/article/10.1007/s10494-014-9576-y.

[26] Eirik Æsøy and James R. Dawnson. *Dataset: A turbulent bluff-body stabilised H2-flame*. 2023. URL: https://tnfworkshop.org/wp-content/uploads/2023/05/Description_NTNU_BB_H2_Flame.pdf.

[27] Alessandro Porcarelli and Ivan Langella. "Mitigation of preferential diffusion effects by intensive strain in lean premixed hydrogen flamelets". In: *Proceedings of the Combustion Institute* 40.1 (2024), p. 105728. ISSN: 1540-7489. DOI: https://doi.org/10.1016/j.proci.2024.105728. URL: https://www.sciencedirect.com/science/article/pii/S1540748924005364.